Figure 1.

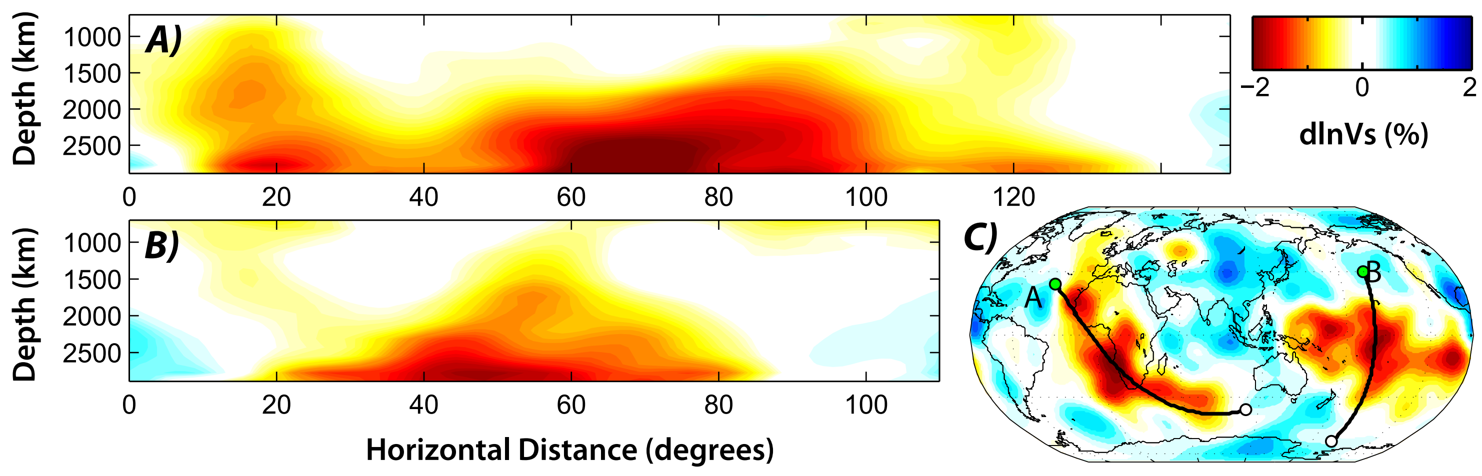
A)
B)
C)
Depth (km)
1000
1500
2000
2500
0
20
40
60
80
100
120
Horizontal Distance (degrees)
−2
0
2
dlnVs (%)
A
B

Figure 2.

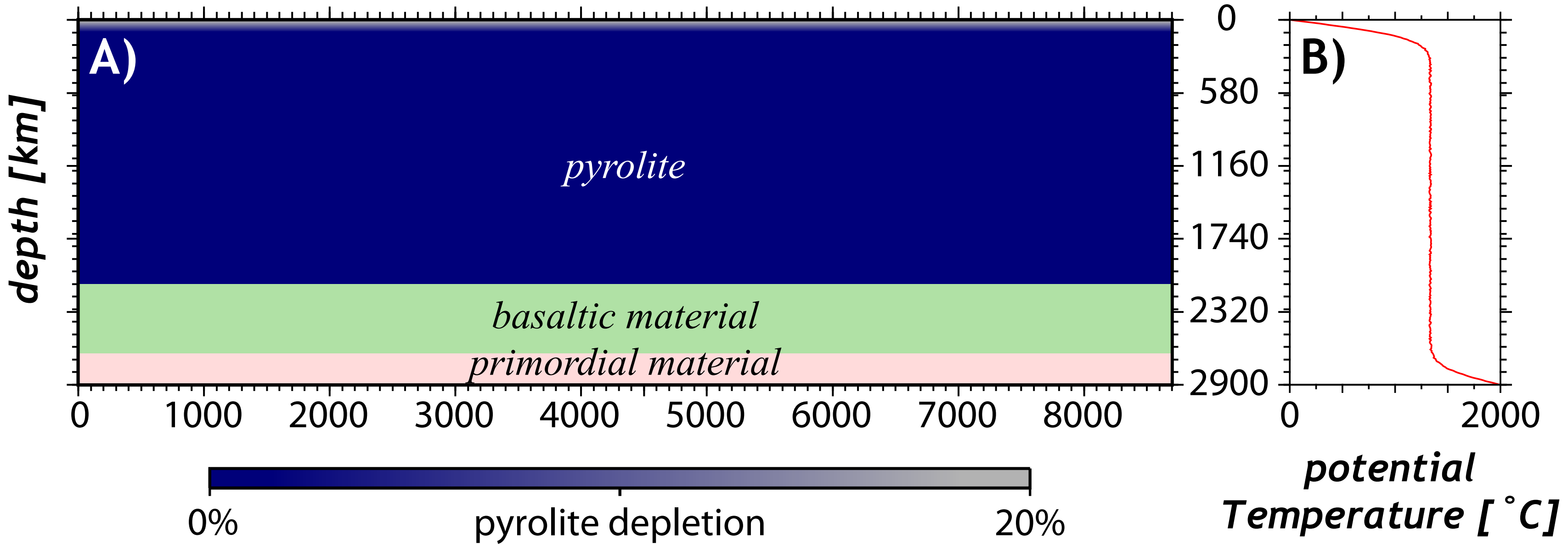

A)
pyrolite
basaltic material
primordial material
depth [km]
0
580
1160
1740
2320
2900
0
1000
2000
3000
4000
5000
6000
7000
8000
0%
pyrolite depletion
20%
B)
0
2000
potential Temperature [˚C]

Figure 3.

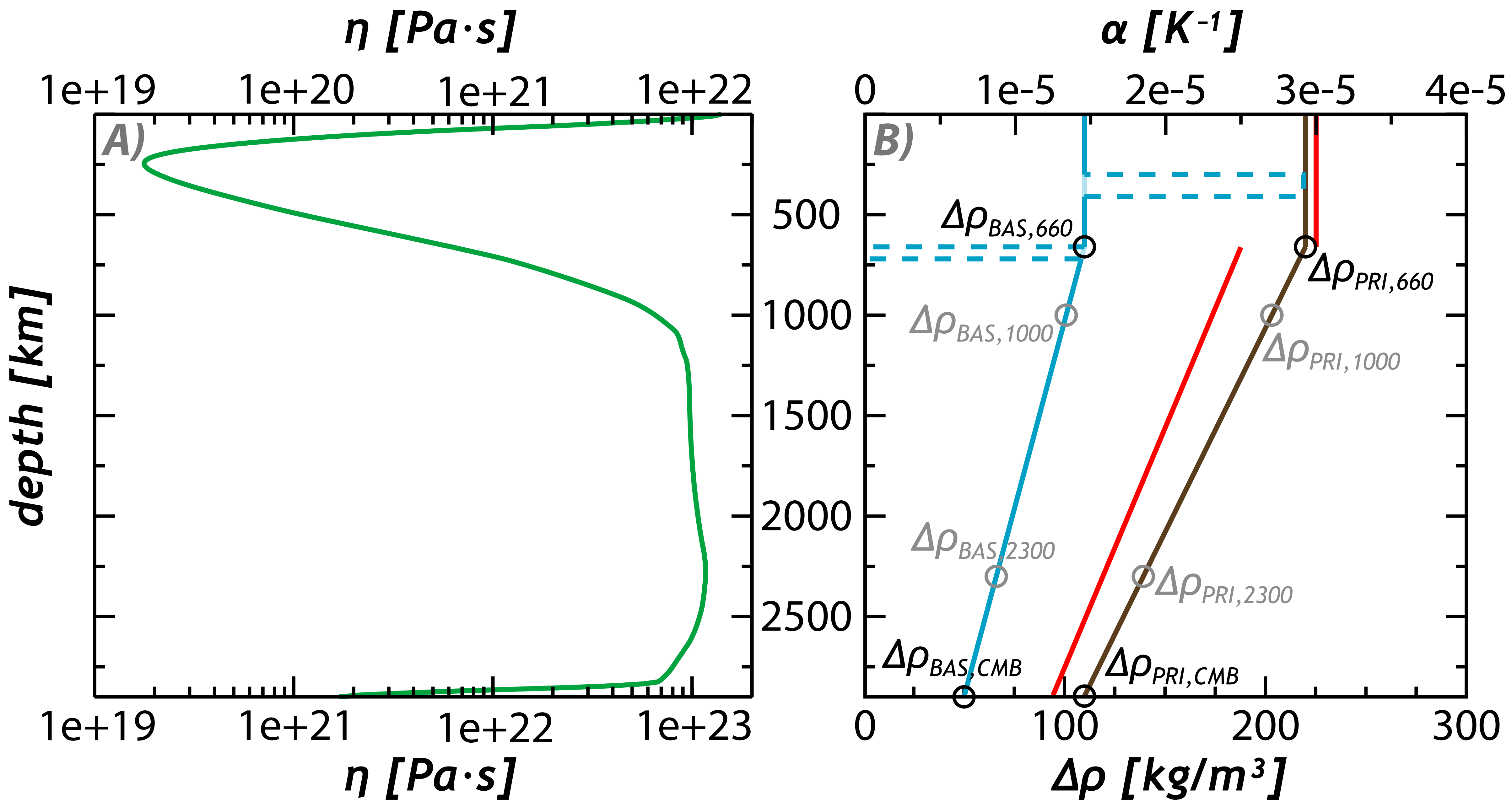

η [Pa·s]
1e+19
1e+20
1e+21
1e+22
A)
depth [km]
500
1000
1500
2000
2500
1e+19
1e+21
1e+22
1e+23
η [Pa·s]
α [K⁻¹]
0
1e-5
2e-5
3e-5
4e-5
B)
Δρ_BAS,660
Δρ_PRI,660
Δρ_BAS,1000
Δρ_PRI,1000
Δρ_BAS,2300
Δρ_PRI,2300
Δρ_BAS,CMB
Δρ_PRI,CMB
0
100
200
300
Δρ [kg/m³]

Figure 4.

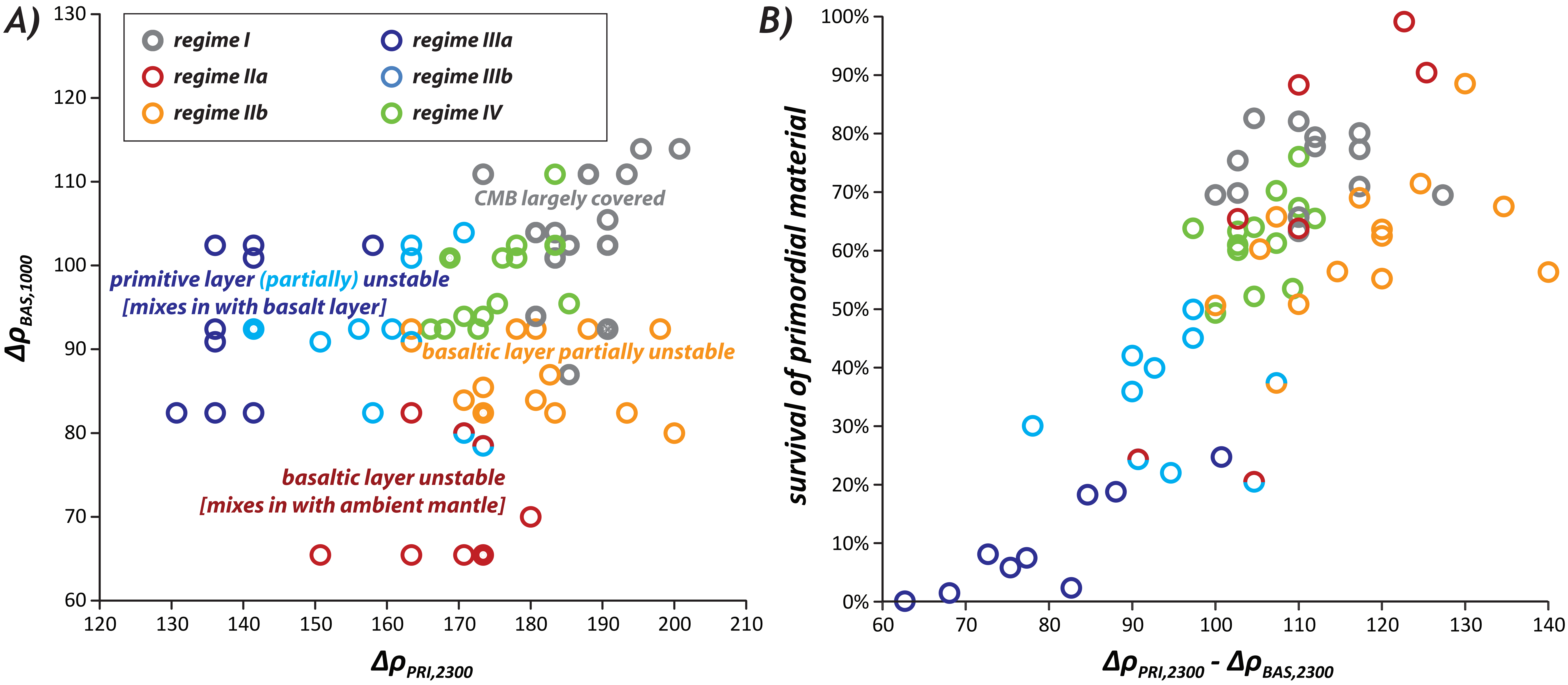

A)
B)
regime I
regime IIa
regime IIb
regime IIIa
regime IIIb
regime IV
CMB largely covered
primitive layer (partially) unstable
[mixes in with basalt layer]
basaltic layer partially unstable
basaltic layer unstable
[mixes in with ambient mantle]
$\Delta\rho_{BAS,1000}$
$\Delta\rho_{PRI,2300}$
survival of primordial material
$\Delta\rho_{PRI,2300} - \Delta\rho_{BAS,2300}$

Figure 5.

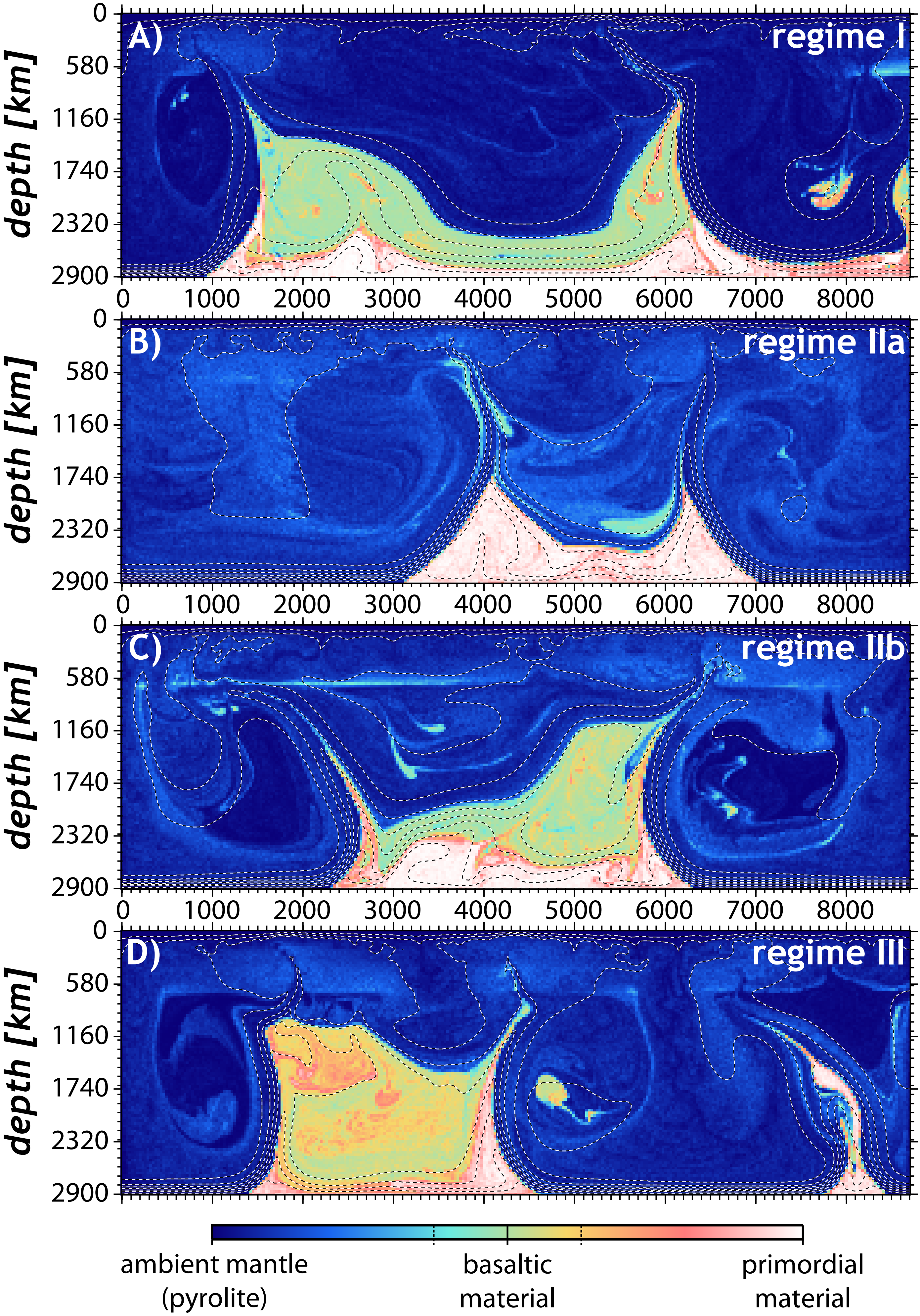

A)
regime I
B)
regime IIa
C)
regime IIb
D)
regime III
depth [km]
0
580
1160
1740
2320
2900
0
1000
2000
3000
4000
5000
6000
7000
8000
ambient mantle
(pyrolite)
basaltic
material
primordial
material

Figure 6.

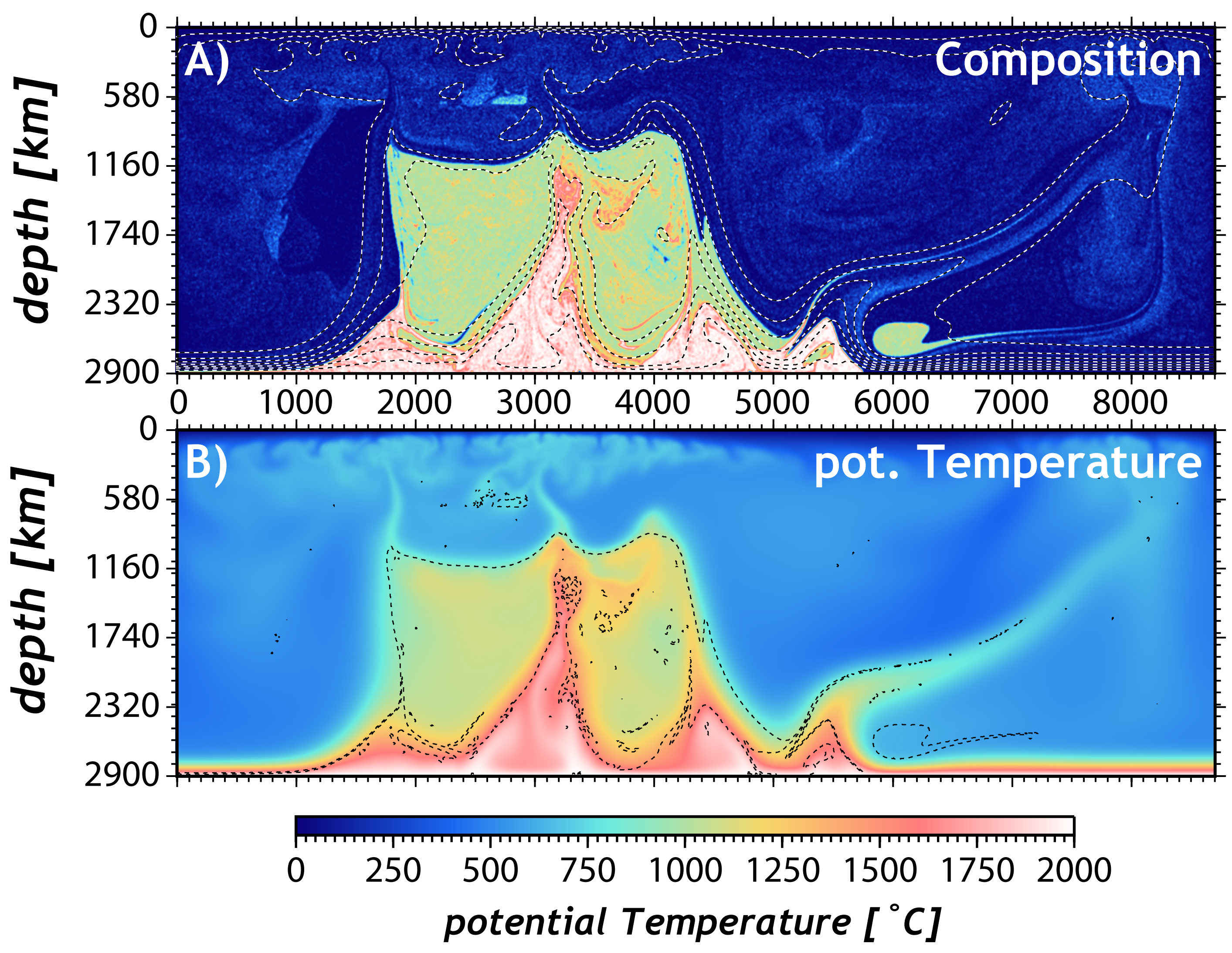
A)
Composition
B)
pot. Temperature
depth [km]
0
580
1160
1740
2320
2900
0
1000
2000
3000
4000
5000
6000
7000
8000
0
250
500
750
1000
1250
1500
1750
2000
potential Temperature [˚C]

Figure 7.

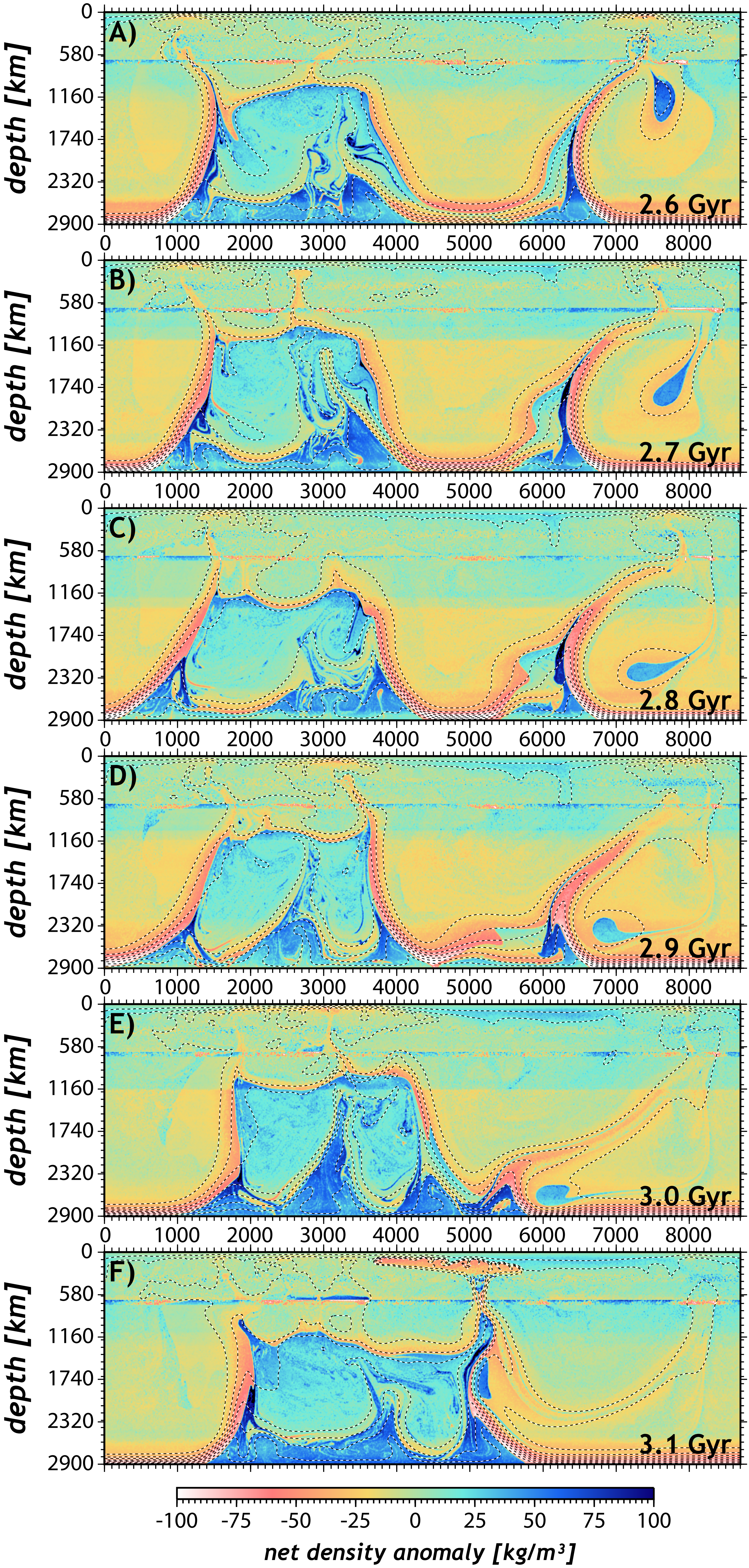
A)
B)
C)
D)
E)
F)
2.6 Gyr
2.7 Gyr
2.8 Gyr
2.9 Gyr
3.0 Gyr
3.1 Gyr
depth [km]
0
580
1160
1740
2320
2900
0 1000 2000 3000 4000 5000 6000 7000 8000
-100 -75 -50 -25 0 25 50 75 100
net density anomaly [kg/m³]

Figure 8.

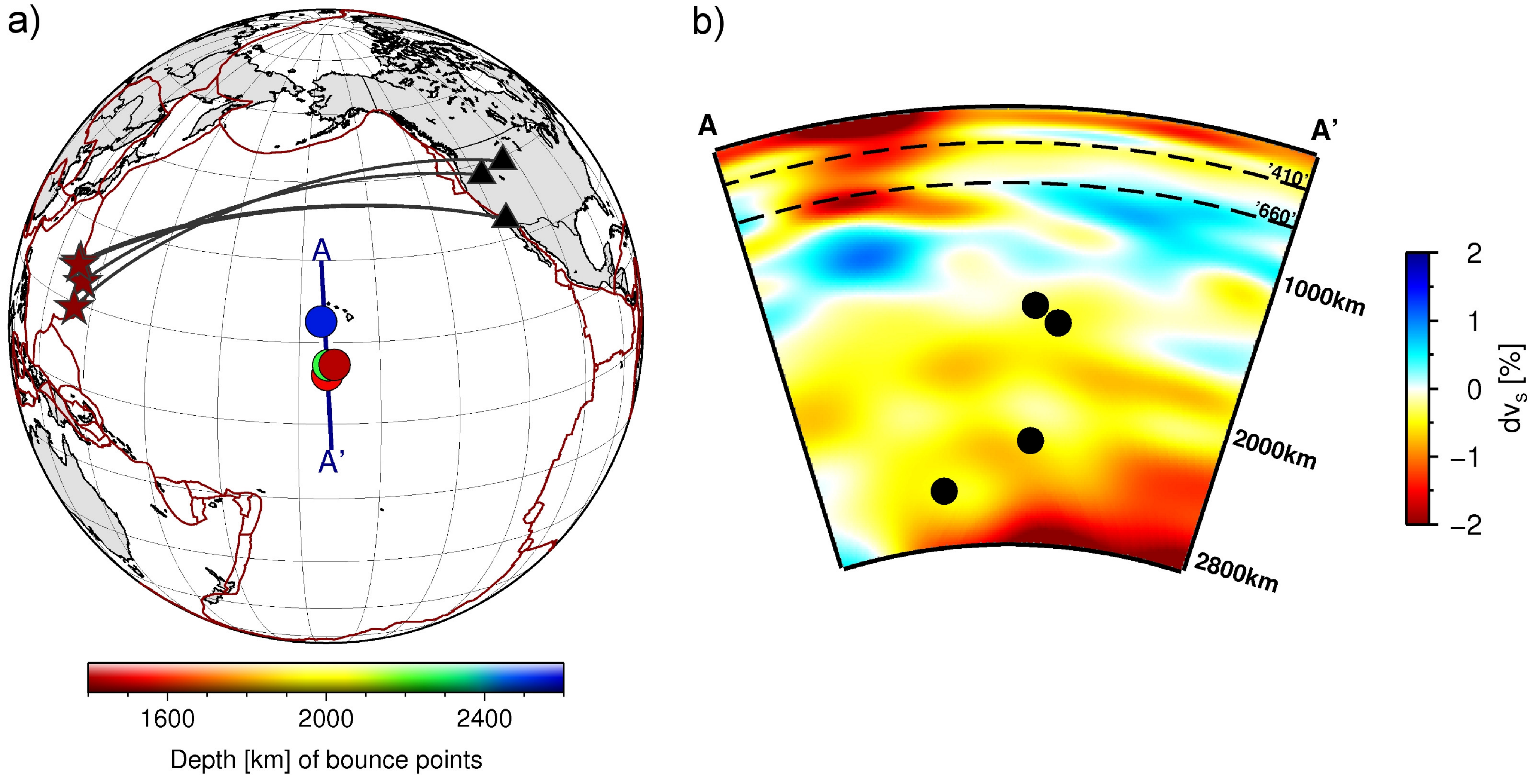

a)
A
A'
1600
2000
2400
Depth [km] of bounce points
b)
A
A'
'410'
'660'
1000km
2000km
2800km
2
1
0
−1
−2
dv$_S$ [%]

Figure 9.

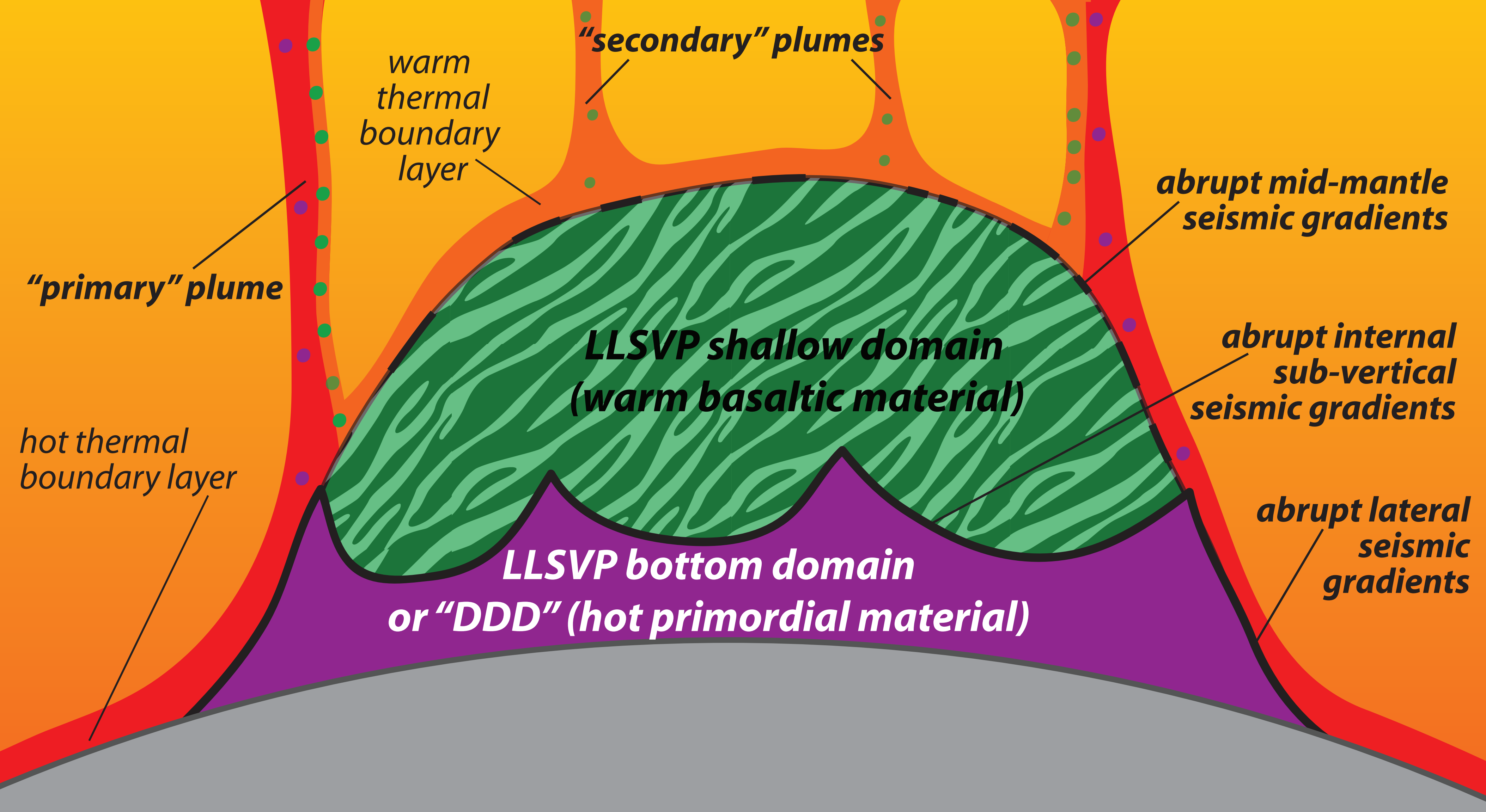
"secondary" plumes
warm thermal boundary layer
"primary" plume
abrupt mid-mantle seismic gradients
LLSVP shallow domain (warm basaltic material)
abrupt internal sub-vertical seismic gradients
hot thermal boundary layer
abrupt lateral seismic gradients
LLSVP bottom domain or "DDD" (hot primordial material)

Compositional layering within the Large Low Shear-wave Velocity Provinces in the lower mantle

Maxim D. Ballmer[1,2]*, Lina Schumacher[3], Vedran Lekic[4], Christine Thomas[3], and Garrett Ito[5]

(1) Institut für Geophysik, Departement für Erdwissenschaften, ETH Zürich, 8092 Zürich, Switzerland,
(2) Earth-Life Science Institute, Tokyo Institute of Technology, Meguro, Tokyo 152-8551, Japan,
(3) Institut für Geophysik, Westfälische Wilhelms Universität Münster, 48149 Münster, Germany,
(4) Department of Geology, University of Maryland, College Park, MD 20742, USA, (5) School of Ocean and Earth Sciences and Technology, University of Hawai‘i at Manoa, Honolulu, HI 96822, USA,
(*) corresponding author: maxim.ballmer@erdw.ethz.ch

Abstract

The large low shear-wave velocity provinces (LLSVP) are thermochemical anomalies in the deep Earth's mantle, thousands of km wide and ~1,800 km high. This study explores the hypothesis that the LLSVPs are compositionally subdivided into two domains: a primordial bottom domain near the core-mantle boundary and a basaltic shallow domain extending from 1,100~2,300 km depth. This hypothesis reconciles published observations in that it predicts that the two domains have different physical properties (bulk-sound vs. shear-wave speed vs. density anomalies), the transition in seismic velocities separating them is abrupt, and both domains remain seismically distinct from the ambient mantle. We here report underside reflections from the top of the LLSVP shallow domain, supporting a compositional origin. By exploring a suite of two-dimensional geodynamic models, we constrain the conditions under which well-separated "double-layered" piles with realistic geometry can persist for billions of years. Results show that long-term separation requires density differences of ~100 kg/m^3 between LLSVP materials, providing a constraint for origin and composition. The models further predict short-lived "secondary" plumelets to rise from LLSVP roofs and to entrain basaltic material that has evolved in the lower mantle. Long-lived, vigorous "primary" plumes instead rise from LLSVP margins and entrain a mix of materials, including small fractions of primordial material. These predictions are consistent with the locations of hotspots relative to LLSVPs, and address the geochemical and geochronological record of (oceanic) hotspot volcanism. The study of large-scale heterogeneity within LLSVPs has important implications for our understanding of the evolution and composition of the mantle.

1. Introduction

Thermochemical structures in the deep mantle bear witness of the Earth's thermal and chemical evolution, and reflect large-scale mantle convection patterns. Seismic shear-wave and P-wave tomography reveals two antipodal large low shear-wave velocity provinces (LLSVP) in the lowermost mantle, one beneath the Pacific and the other beneath Africa (e.g., *Dziewonski et al.*, 2010). LLSVP locations are spatially correlated with ancient and modern hotspots, and hence thought to play a key role in the generation of mantle plumes (*Torsvik et al.*, 2006; *Burke et al.*, 2008; *Torsvik et al.*, 2010; *Austermann et al.*, 2014; *Davies et al.*, 2015; *Doubrovine et al.*, 2016). Indeed, both LLSVPs are associated with broad dynamic topography anomalies at the surface ("Superswells") that have been linked to large-scale mantle upwelling. LLSVPs have been identified as potential geochemical reservoirs for materials that are sampled by hotspots (e.g., *Christensen and Hofmann*, 1994).

Each of the LLSVPs is thousands of km wide and extends from the core-mantle boundary (CMB, at 2,900 km depth) to mid-mantle (i.e., ~1,100 km) depths. As shown by Figure 1, such a large depth extent of the LLSVPs is supported by seismic tomography models (e.g., *Tanaka et al.*, 2009; *Ritsema et al.*, 2011; *Cottaar and Lekic*, 2016), but somewhat remains a semantic issue that depends on the definition of LLSVPs (see below). Using cluster analysis, *Cottaar and Lekic* (2016) demonstrate that five different shear-wave velocity models agree well with each other in terms of the geometry and depth extent of "slow clusters" (i.e. LLSVPs according to our definition here; see their Figs. 4-5). Based on observations of abrupt lateral gradients in seismic velocity across their boundaries (*Ni et al.*, 2002; *Ni and Helmberger*, 2003; *To et al.*, 2005; *He and Wen*, 2009; *Kawai and Geller*, 2010; *Sun and Miller*, 2013; *Thorne et al.*, 2013), anti-correlation between shear-wave and bulk-sound velocity (v_s and v_Φ) anomalies (*Su and Dziewonski*, 1997; *Masters et al.*, 2000; *Romanowicz*, 2001; *Trampert et al.*, 2004; *Mosca et al.*, 2012; *Koelemeijer et al.*, 2016; *Tesoniero et al.*, 2016), as well as decorrelation of v_s with density anomalies (*Ishii and Tromp*, 1999; *Simmons et al.*, 2010; *Mosca et al.*, 2012; *Moulik and Ekström*, 2016), a purely thermal origin of LLSVPs remains unlikely. In turn, LLSVPs are commonly interpreted as being hot but compositionally dense piles that are shaped by ambient-mantle convection (*Davaille*, 1999; *McNamara and Zhong*, 2005; *Tan and Gurnis*, 2007; *Deschamps and Tackley*, 2008; *Steinberger and Torsvik*, 2012).

Two end-member scenarios have been proposed for LLSVP composition and origin. First, (1) LLSVPs may dominantly consist of subducted oceanic crust (or MORB) that has largely segregated from harzburgite to accumulate in the deep mantle over geologic timescales (*Christensen and Hofmann*, 1994; *Xie and Tackley*, 2004; *Nakagawa and Tackley*, 2005; *Brandenburg and van Keken*, 2007). Depending on the efficiency of segregation, such a "basaltic material" may also contain some small fraction of harzburgite. Second, (2) LLSVPs may be composed of "primordial" materials, formed early in Earth's history (*Deschamps et al.*, 2012; *Li et al.*, 2014; *Nakagawa and Tackley*, 2014). For example, compositional fractionation during magma-ocean crystallization may have created large-scale density anomalies that are too strong to be fully homogenized during billions of years of mantle convection (*Labrosse et al.*, 2007; *Brown et al.*, 2014). Similarly, subducted (or foundered) Hadean proto-crust may have persisted at the base of the mantle to contribute to the formation of LLSVPs (*Boyet and Carlson*, 2005; *Tolstikhin et al.*, 2006). Noble-gas isotope signatures of hotspot lavas as well as well gases support the existence of primordial reservoirs somewhere in the mantle (*Mukhopadhyay*, 2012; *Peto et al.*, 2013; *Caracausi et al.*, 2016), possibly spatially related to plume-source regions.

Furthermore, seismic evidence indicates that compositional heterogeneity is present *within* the LLSVPs (Fig. 1). For example, the relatively shallow domain of the LLSVP is characterized by moderately negative v_s (about -0.5% to -1% on average) in seismic tomography models, whereas the bottom domain is characterized by much greater negative anomalies (*Hernlund and Houser*, 2008; *Lekic et al.*, 2012). The robustness of this observation is indicated by an excellent agreement among tomography models (*Cottaar and Lekic*, 2016), and an extensive illumination of LLSVPs by S-waves. The average transitional depth between domains is at ~2,300 km, or ~600 km above the CMB. Abrupt vertical velocity gradients (in both v_p and v_s) have been detected by waveform analyses in a similar depth range (2,200~2,500 km) (*He and Wen*, 2009; *Kawai and Geller*, 2010; *Sun and Miller*, 2013; *Frost and Rost*, 2014), suggesting the transition between domains reflects a compositional boundary. Hereinafter, we refer to the LLSVP bottom domain as "Distinct Deep Domain", or DDD. Note that in the literature there is some ambiguity in terms of the definition of the LLSVP. While the definition of the LLSVP in some papers (e.g., *Hernlund and Houser*, 2008; *Deschamps et al.*, 2012) is equivalent to that of the DDDs here, we here refer to the LLSVPs in a broader sense (i.e. extending from the CMB to ~1,100 km depth; see Fig. 1). For example, LLSVPs make up ~8% of the mantle's volume according to our definition (*Cottaar and Lekic*, 2016); the DDDs make up 2%-3% (*Hernlund and Houser*, 2008).

If these systematic changes of seismic properties across LLSVPs indeed indicate an internal compositional boundary at 2,200~2,500 km depth, then any further study may yield insight into the origin of materials that evolve deep in the mantle, and are recycled by upwelling plumes. For example, the LLSVP shallow domain may be made up of basaltic materials or hot pyrolite (i.e., purely thermal origin). DDDs may host primordial materials, or a mix of primordial and basaltic materials (*Tackley*, 2012). The presence of primordial materials within DDDs is supported by the observed anti-correlation between v_s and v_Φ, which is difficult to be explained by the presence of basalt (and high-pressure polymorphs) alone (*Deschamps et al.*, 2012). A composite primordial-basaltic reservoir in the mantle can further account for the geochemical signature of plume-fed magmatism at major hotspots (e.g., *Garapic et al.*, 2015). Whereas geodynamic studies of a dense layer in the deep mantle have significantly advanced our understanding of LLSVPs (*McNamara and Zhong*, 2005; *Tan and Gurnis*, 2007; *Bower et al.*, 2013; *Bull et al.*, 2014; *Li et al.*, 2014; *Nakagawa and Tackley*, 2014), heterogeneity within this layer has not been studied systematically.

In this study, we investigate the geodynamical, geochemical and seismological implications of large-scale compositional heterogeneity within LLSVPs. We use high-resolution two-dimensional geodynamic models to explore the conditions under which compositional layering within thermochemical structures can be preserved over geologic timescales. LLSVP compositional models are evaluated by comparing model predictions with published seismic observations, as well as with newly identified out-of-plane seismic reflections in the mid-Pacific. Finally, we compare the predictions of our geodynamic models in terms of plume generation in the lower mantle with the geochemical and geographical record of intraplate hotspot volcanism.

2. Numerical Methods

To model heat and material transport through the mantle, we solve the conservation equations of mass, momentum and energy with the incompressible Boussinesq approximation using the finite-element code CitcomCU (*Moresi and Gurnis*, 1996; *Zhong*, 2006). We use a significantly extended version of CitcomCU that can robustly solve for thermochemical convection (*van Hunen et al.*, 2005; *Ballmer et al.*, 2009; 2010). Compositional properties are advected by passive markers, or "tracers" (*Gerya and Yuen*, 2003). Any non-linear feedback effects of thermochemical convection are addressed by using a second-order Runge-Kutta time-integration scheme (*Ballmer et al.*, 2009).

The rectangular two-dimensional numerical model domain is z_{box} = 2,900 km deep and x_{box} = 8,700 km wide, with a resolution of 320 x 1024 elements. Refinement of the vertical dimension of the grid in the upper mantle slightly enhances the resolution in the upper mantle (i.e., 8.25 km) compared to the lower mantle (i.e., 9.333 km).

Velocity boundary conditions involve free-slip on all boundaries except for the top, where velocities are set to zero (Fig. 2). No flow into or out of the box is allowed. Imposing a no-slip condition at the top reduces computational time, while having no significant impact on results. Tests show that the choice of the top velocity boundary condition neither affects the root-mean square velocities in the box, nor the distribution of materials after several billion years model time.

Thermal boundary conditions involve a fixed potential temperature of T_m = 2,000 °C at the bottom, and T_0 = 0 °C at the top. These conditions impose a superadiabatic temperature difference of T_m between the CMB and surface. The bottom thermal boundary condition corresponds to a "real" CMB temperature of ~3,000 °C, depending on the assumed geotherm (which is not prescribed here). Such a CMB temperature is well within, but near the low end of the range of estimates (*Lay et al.*, 2008), but according to recent mineral-physics constraints any higher values would likely require large-scale melting in the deepest mantle (*Nomura et al.*, 2014), which is inconsistent with seismic data. Geotherms with relatively low T_m are also generally consistent with one-dimensional seismic models such as PREM (*Deschamps and Trampert*, 2004; *Mosca et al.*, 2012). As the modeled mantle is purely heated from the bottom with no internal heating (and as the CMB area remains overestimated in Cartesian models of mantle convection), the modelled CMB heat-flux is an upper bound and hence so are the density anomalies required to stabilize thermochemical layers in the deep mantle (i.e., despite our conservative choice of T_m).

Initial thermal conditions involve a mid-mantle potential temperature of 1,333.3 °C with boundary layers at the top and bottom. Thermal boundary layers are computed as 80-Myr half-space cooling profiles. A small thermal random noise is added to the initial temperature field. In any case, we find that model results are insensitive to the initial thermal condition.

The compositional field involves three major components. (1) Pyrolite is the typical upper-mantle rock (*Workman and Hart*, 2005), similar in composition to lherzolite (and high-pressure polymorphs). We refer to (2) "basaltic material" as a fine-scale mixture of mostly mafic (e.g., high-pressure polymorphs of MORB) and some ultramafic mantle rocks (e.g., lherzolite or harzburgite). We refer to (2) "primordial material" as being formed during the first ~100 Myrs of Earth's history, and to have remained mostly unprocessed by subsequent mantle melting or metasomatism, but do not impose a specific composition (see discussion section). Whereas the models are designed to simulate these three materials (according to our final interpretations, see below), our results only depend on the material properties modelled.

The compositional field is initially three-layered and stably stratified (Figure 2). The primordial layer initially extends from the CMB to 250 km above the CMB, the basaltic layer extends from 250 km above the CMB to 2,100 km depth, and pyrolite makes up most of the rest of the mantle. In the sublithospheric mantle and lithosphere, the composition is all pyrolite at ~100 km depth and then transitions to all harzburgite at the surface (Fig. 2). This transition represents the depletion of pyrolite due to partial melting as calculated from a separate numerical model of mid-ocean ridge melting according to Ballmer et al. (2009). Note however that depleted pyrolite largely remains in the nearly stationary lithosphere through model evolution; its presence does not have any important effects on model results.

By initially imposing the modeled materials as layers, we focus on studying the stability and entrainment of basaltic and primordial materials in the lower mantle. While an initial condition with a layer of primordial material near the base of the mantle is realistic (i.e., following e.g. a global-scale gravitational cumulate overturn (*Elkins-Tanton et al.*, 2005), or basal-magma ocean freezing (*Labrosse et al.*, 2007)), MORB is more likely to have progressively accumulated in the lower mantle as a consequence of deep subduction. Since the mechanisms for MORB-harzburgite separation remain ill-constrained, we choose not to explicitly model the processes of deep subduction and segregation. Uncertainties in the efficiency of this segregation are reflected by the density anomaly of the initially imposed layer of basaltic material, which is varied as a free model parameter (see below). Variable densities of the basaltic material thereby reflect the content of ultramafic components within the dominantly basaltic mechanical mixture. In addition, these densities reflect the specific composition in major oxides of the mafic component (i.e., MORB) itself, which may have important effects on dynamics (*Nakagawa et al.*, 2010).

In our thermochemical models, lateral density variations due to thermal and compositional anomalies drive mantle flow:

$$\rho = \rho_0 - \alpha(T - T_{\mathrm{m}})\rho_0 + X_{PRI}\Delta\rho_{PRI} + X_{BAS}\Delta\rho_{BAS} + F\Delta\rho_F, \quad (1)$$

with ρ density; ρ_0 reference density; T temperature; α thermal expansivity; F depletion of pyrolite; X_{BAS} and X_{PRI} volume fractions of basaltic and primordial material, respectively; and $\Delta\rho_{BAS}$, $\Delta\rho_{PRI}$ and $\Delta\rho_F$ the density anomalies related to these two materials and depleted pyrolite, respectively. Note that $\Delta\rho_{BAS}$ and $\Delta\rho_{PRI}$ are positive, whereas $\Delta\rho_F$ is negative (-100 kg/m^3). According to the objectives of this study, we carefully account for the depth dependency of thermal expansivity α, as well as of the density anomalies related to basaltic and primordial material ($\Delta\rho_{BAS}$ and $\Delta\rho_{PRI}$) in the lower mantle (Fig. 3). α is fixed in the upper mantle at $3.0\cdot10^{-5}$ K^{-1} and linearly decreases with depth in the lower mantle (from $2.5\cdot10^{-5}$ K^{-1} at 660 km depth to $1.25\cdot10^{-5}$ K^{-1} at the CMB), generally consistent with Tosi et al. (2013). In the upper mantle, $\Delta\rho_{BAS}$ and $\Delta\rho_{PRI}$ are set to $\Delta\rho_{BAS,UM}$ and $\Delta\rho_{PRI,UM}$, respectively, except for the depth range of 300 km to 410 km, where $\Delta\rho_{BAS}$ is set to $2\Delta\rho_{BAS,UM}$ (*Aoki and Takahashi*, 2004). In the lower mantle, $\Delta\rho_{BAS}$ and $\Delta\rho_{PRI}$ linearly decrease from $\Delta\rho_{BAS,UM}$ to $\Delta\rho_{BAS,CMB}$ and $\Delta\rho_{PRI,UM}$ to $\Delta\rho_{PRI,UM}$, respectively, except for the depth range of 660-720 km where $\Delta\rho_{BAS}$ is set to $-3\Delta\rho_{BAS,UM}$ (*Hirose et al.*, 1999; *Xu et al.*, 2008). In this depth range, $\Delta\rho_F$ is also reversed to +100 kg/m^3. $\Delta\rho_{BAS,UM}$, $\Delta\rho_{BAS,CMB}$, $\Delta\rho_{PRI,UM}$ and $\Delta\rho_{PRI,CMB}$ are free model parameters. Accordingly, we explore the effects of variations in density as well as compressibility (or $\partial\rho/\partial z$) of both basaltic and primordial materials on thermochemical mantle convection.

In our simplified models, mantle viscosity η depends on temperature and depth only:

$$\eta = \eta_0 \exp\left(\frac{E^* + \rho_0 g z V^*}{RT} - \frac{E^*}{RT_m}\right), \quad (2)$$

with η_0, g, z, E^*, V^* and R reference viscosity, gravity acceleration, depth, activation energy, activation volume and the ideal gas constant, respectively. Applying even just our conservative choices for E^* and V^*, viscosity contrasts over the full mantle temperature and depth range reach eight and five orders of magnitude, respectively. The total viscosity contrast across the model domain is cut off (at six orders of magnitude) to ensure numerical stability, and to limit the strength of the upper lithosphere, which in nature deforms plastically. The specific cutoffs (at $1.4\cdot10^{17}$ Pa·s, and $1.4\cdot10^{23}$ Pa·s) are chosen such that mantle upwellings are better resolved than downwellings. Downwellings are rather diffuse and not slab-like, but note that the rheology of downwellings in the deep mantle, i.e. where they interact with thermochemical piles, remains poorly understood. A viscosity jump at 660 km depth is not explicitly modeled, but the imposed dependency of viscosity on depth (and temperature) creates a realistic average viscosity profile (Fig. 3a) (*Rudolph et al.*, 2015). According to the effective upper-mantle and lower-mantle viscosities in our models, the effective Rayleigh numbers in are $\sim 2.6 \cdot 10^8$ and $\sim 1.2 \cdot 10^6$, respectively. All other parameters are chosen to represent the conditions of the lower mantle (Table 1), the dynamics of which we focus on in this study.

In the model suite, we specifically explore ~70 cases with different $\Delta\rho_{BAS,UM}$, $\Delta\rho_{BAS,CMB}$, $\Delta\rho_{PRI,UM}$ and $\Delta\rho_{PRI,CMB}$ (see Table 1, Fig. 3b). The initial condition (e.g. initial volumes of basaltic and primordial materials; Fig. 2) and other parameters (see methods) remain fixed. Thereby, we focus on investigating the effects of the intrinsic density anomalies of basaltic and primordial materials relative to the (less dense) pyrolite, as well as the slopes of their depth-dependencies in the lower mantle:

$$\partial\Delta\rho_{BAS}/\partial z = (\Delta\rho_{BAS,UM} - \Delta\rho_{BAS,CMB})/h_{LM}$$

and

$$\partial\Delta\rho_{PRI}/\partial z = (\Delta\rho_{PRI,UM} - \Delta\rho_{PRI,CMB})/h_{LM}$$

with lower mantle height h_{LM} = 2,900 km – 660 km. We chose to vary the above four parameters, because they are ill-constrained due to mineral-physics uncertainties (*Deschamps et al.*, 2012) and have been shown to have first-order effects on thermochemical convection (*Tan and Gurnis*, 2005; 2007). Note that $\partial\Delta\rho_{BAS}/\partial z$ and $\partial\Delta\rho_{PRI}/\partial z$ are directly related to (and thus representative of) relevant physical properties. They are generally proportional to the compressibilities of basaltic and primordial materials in the lower mantle, respectively, and inversely proportional to their bulk moduli.

Geodynamic models were run for simulation times of at least 3 Gyr, to approach a statistical steady state. We refrain from running the models for much longer timescales (e.g. ~4.5 Gyrs), because the style of surface tectonics and mantle convection in the early Earth remains poorly understood. Also given the boundary conditions (see above) and fixed parameters (Table 1), which are inspired by modern-mantle values, our numerical experiments represent near steady-state models of modern-mantle dynamics rather than mantle evolution models.

3. Results of Numerical Models

As a function of model parameters, four regimes of thermochemical convection in the deep mantle are manifested (Fig. 4). In regime I, the primordial (and basaltic) material covers most of the CMB in a nearly continuous layer. In regime II, thermochemical piles emerge mostly consisting of primordial material at the bottom plus variably small volumes of basaltic material at the top, but there is significant mixing of basaltic and pyrolytic material. In regime III, thermochemical piles also emerge, but separation between basaltic and primordial material within these piles does not persist for geological timescales. In regime IV, the basaltic and primordial layers together form a “double-layered” thermochemical pile (leaving large areas of the core-mantle boundary uncovered) with two separate compositional domains. The regimes are described in detail in sections 3.1-3.2 and Figures 5-7. The criteria used to distinguish between these regimes are the coverage of the CMB by primordial material, and the persistence of coherent domains of primordial and basaltic materials after 3 Gyrs model time (see Table 2).

The sensitivity of these different regimes on model parameters is visualized in Figure 4a as a regime map in terms of two key quantities: (1) A measure of $\Delta\rho_{PRI}$ in the deep mantle, here evaluated at 2,300 km depth (i.e., near DDD tops; $\Delta\rho_{PRI,2300} = 0.268\Delta\rho_{PRI,660} + 0.732\Delta\rho_{PRI,CMB}$), and (2) a measure of $\Delta\rho_{BAS}$ in the mid-mantle, here evaluated at 1,000 km depth (i.e., near LLSVP tops; $\Delta\rho_{BAS,1000} = 0.848\Delta\rho_{BAS,660} + 0.152\Delta\rho_{BAS,CMB}$). High $\Delta\rho_{PRI}$ in the deep mantle (i.e., high $\Delta\rho_{PRI,2300}$) promotes efficient settling of primordial material at the CMB (regime I). For low-to-moderate $\Delta\rho_{BAS}$ in the mid-mantle (i.e., low-to-moderate $\Delta\rho_{BAS,1000}$), the basaltic layer is readily entrained, and thus partially or completely lost over timescales of hundreds of millions to billions of years (regime II). For low $\Delta\rho_{PRI,2300}$, mixing between the primordial and basaltic layers occurs (regime III), mostly promoted by a small difference between $\Delta\rho_{PRI}$ and $\Delta\rho_{BAS}$ neat the CMB (Fig. 4b). For the remaining parameter space with intermediate $\Delta\rho_{PRI}$ and $\Delta\rho_{BAS}$, “double-layered” thermochemical piles persist for >3 Gyrs model time (regime IV).

3.1 Thermochemical convection in the deep mantle (regimes I-III):

Figure 5a shows an example case for regime I (case X5LH). In regime I, the drag exerted by mantle convection is insufficient to significantly pile up the hot primordial material due to high $\Delta\rho_{PRI,2300}$ (and $\Delta\rho_{PRI,CMB}$). Instead, the primordial material forms an almost continuous layer at the CMB with some topography (heights ranging from ~150 km to ~600 km), and the basaltic material piles up on top of this layer. In some cases, even the basaltic material covers part of the CMB. Regime I is manifested for $\Delta\rho_{PRI,2300}$ > ~180 kg/m^3 and high $\Delta\rho_{BAS}$ (grey circles in Fig. 4a). High $\Delta\rho_{BAS}$ in addition to high $\Delta\rho_{PRI}$ are required, because at low $\Delta\rho_{BAS}$ thermochemical convection switches to regime II, in which the basaltic load is removed from the primordial layer due to entrainment (see below) such that CMB coverage is ultimately reduced.

In regime II, basaltic material is entrained by ambient mantle convection and progressively eroded from the thermochemical piles (see Fig. 5b-c). Thereby, the rate of erosion is a function of model parameter $\Delta\rho_{BAS,1000}$. In sub-regime IIa ($\Delta\rho_{BAS,1000}$ < ~80 kg/m^3), positive (i.e. destabilizing) thermal buoyancy overcomes negative compositional buoyancy, and strong erosion occurs due to gravitational instability. For example, we observe that large chunks of the basaltic layer episodically rise as a whole in case 74KF (see Fig. 5b; red circles in Fig. 4a). In sub-regime IIb ($\Delta\rho_{BAS,1000}$ < ~90 kg/m^3), moderate erosion occurs, mainly due to entrainment by plumes, and a significant amount of basaltic material survives even after 3 Gyrs model time (e.g., case 94KF in Fig. 5c; yellow circles in Fig. 4a). This surviving material forms a layer on top of the primordial material. In both sub-regimes, any eroded basaltic material undergoes convective mixing to be dispersed through the mantle. In many cases, it tends to accumulate in the transition zone, which acts as a "density trap" for basalt (*Nakagawa and Buffett*, 2005; *Ballmer et al.*, 2015b).

In regime III, mixing between primordial and basaltic materials occurs due to a relatively small density difference between those two materials in the deep mantle. For $\Delta\rho_{PRI,2300} - \Delta\rho_{BAS,2300} <$ ~100 kg/m^3, the thermal buoyancy of hot primordial material is sufficient to overcome its intrinsic negative buoyancy, at least relative to the basaltic material (Fig. 5d). Figure 4b shows that $\Delta\rho_{PRI,2300} - \Delta\rho_{BAS,2300}$ controls the rate of mixing (or the amount of primordial material that can remain relatively "pure" after 3 Gyrs model time). Depending on parameters, we find that thermochemical structures in regime III range from partially mixed piles (sub-regime IIIb; see example case X5JB in Fig. 5d; light blue circles in Fig. 4) to fully mixed piles with a more-or-less homogenous distribution of basaltic and primordial material throughout the whole pile (sub-regime IIIa; dark blue circles in Fig. 4 for $\Delta\rho_{PRI,2300} - \Delta\rho_{BAS,2300} <$ ~90 kg/m^3). Whereas relatively pure primordial material in regimes I, II and IV is usually sufficiently dense to avoid significant erosion, a mix of primordial and basaltic materials (or previously termed "basal mélange" (*Tackley*, 2012)) is commonly entrained by plumes. Therefore, the efficiency of mixing between primordial and basaltic materials (regime III vs. regimes I/II/IV) has important implications for the storage timescales of materials in the deep mantle (see discussion section).

3.2 Double-layered thermochemical piles (regime IV):

For moderate $\Delta\rho_{PRI,2300}$ and $\Delta\rho_{BAS,1000}$ (Regime IV; Fig. 4a), mixing rates between all the three materials modeled are significantly smaller than for regimes II and III (Table 2). Accordingly, only limited mixing between materials occurs over 3 Gyrs model time (e.g. reference case A5LE, see Fig. 6a). The well-preserved basaltic and primordial materials form composite "double-layered" thermochemical piles surrounded by ambient-mantle material (Fig. 4a). The primordial material forms the bottom layer of the double-layered pile. This layer displays significant topography extending from the CMB to about 300-700 km above the CMB. It can intermittently peak at heights of ~1,000 km above the CMB, or higher. The basaltic material accumulates on top of the primordial layer like a huge dome reaching depths of ~1,100 km (or heights of ~1,800 km above the CMB). This vertical extent is time-dependent: due to the competition between thermal and compositional buoyancy forces, as well as variable drag exerted by ambient-mantle convection, the double-layered thermochemical pile oscillates as a whole (see also Davaille et al. (1999)). The basaltic layer is generally hotter than the ambient mantle but cooler than the primordial layer (Fig. 6b).

Figure 7 shows snapshots of net density anomalies for the reference case, combining the positive thermal and negative compositional contributions. These net density anomalies (and not the intrinsic density anomalies $\Delta\rho_{BAS}$ and $\Delta\rho_{PRI}$ alone) ultimately control mantle flow and (together with bulk and shear moduli) seismic velocities. For example, warm colors in Figure 7 mark domains that are relatively buoyant (compared to cold colors). Whereas the bottom primordial layer of the LLSVP is overall significantly denser (by about 50 kg/m^3 for cases in regime IV) than the global average, most of the shallow basaltic layer is only slightly denser than the global average (by ~15 kg/m^3). These model predictions are well within the range of normal-mode constraints (*Ishii and Tromp*, 1999; *Trampert et al.*, 2004; *Moulik and Ekström*, 2016; *Koelemeijer et al.*, in review). Only the very top of the basaltic layer displays a somewhat stronger net-density anomaly (~30 kg/m^3), because $\Delta\rho_{BAS}$ increases upwards ($\Delta\rho_{BAS,UM} > \Delta\rho_{BAS,CMB}$) in most of the cases modeled, consistent with mineral-physics data (*Xu et al.*, 2008; *Ricolleau et al.*, 2010; *Deschamps et al.*, 2012). These vertical changes of net density anomaly within the basaltic layer account for its dome-like shape (see Tan and Gurnis (2005; 2007)). In contrast, vertical changes of net density anomaly across the primordial layer are small (at least compared to the global average), which thus forms ridge-like piles. The configuration and shape of primordial ridge-like piles is strongly time-dependent and sensitive to ambient-mantle flow, consistent with previous work (e.g., *McNamara et al.*, 2010). A thin thermal boundary layer with strongly negative net density anomaly forms at the CMB (i.e., outside the piles), as well as along the flanks of the hot primordial piles. Other thermal boundary layers, somewhat less pronounced, form at the top of the basaltic dome, and along the internal boundary of the composite thermochemical pile.

Two different types of mantle plumes rise from two different thermal boundary layers (see Figs. 6-7 and Movies S1-S3). Vigorous plumes rise out of the hot thermal boundary layers along the flanks of the double-layered thermochemical pile. The bases of these plumes are relatively stationary over long timescales (100s of Myrs), as they are anchored by one of the peripheral ridges of primordial material. They move at rates of less than ~0.3 km/Myr (i.e. relative to LLSVPs, which themselves are inferred to be stationary (*Torsvik et al.*, 2010)). Less vigorous, and somewhat cooler plumes rise from the warm thermal boundary layer at the top of basaltic domes. They are usually short-lived, and their bases move swiftly relative to the LLSVPs (i.e., at rates of up to several km/Myr).

In addition, a major plume pulse occasionally rises out of the thermochemical pile itself (see Figures 7e-f). In the models, a plume pulse is triggered by a combination of ambient mantle flow and build-up of heat within (or near) the pile. Such a pulse can deliver a lot of heat (and potentially basaltic material) into the upper mantle and may support large-scale asthenospheric melting, perhaps to sustain flood-basalt volcanism (see *Lin and van Keken*, 2005; *Sobolev et al.*, 2011b).

4. Comparison of model predictions with seismic constraints

Our geodynamic models predict that hot and compositionally distinct rock forms large piles at the base of the mantle, similar in geometry to LLSVPs as imaged by seismic tomography

(*Cottaar and Lekic*, 2016). In regime I, thermochemical piles are predicted to largely cover the CMB, inconsistent with the footprint of LLSVPs constrained by tomography (i.e., 20%~30% of CMB area, or ~50% in a cross-section along a great circle through both LLSVPs). In regimes IIa and IIIa, piles are predicted to be internally homogeneous in composition. This type of thermochemical convection in the deep mantle, whether containing almost purely primordial piles (IIa) or well-mixed basaltic-primordial piles (IIIa), has been extensively discussed in the literature (see references in *Tackley*, 2012; *Hernlund and McNamara*, 2015). In all other cases, moderately heterogeneous (incipient mixing, regime IIIb) or strongly heterogenous piles are predicted to form. Strongly heterogeneous piles display well-separated layers of basaltic and primordial materials (regimes IIb and IV).

Pronounced compositional heterogeneity within LLSVPs, as predicted for regimes IIb and IV, is supported by seismic constraints. Reflections deep within the Pacific LLSVP cannot be explained by the iso-chemical perovskite to post-perovskite phase transition and hence indicate compositional heterogeneity (*Cobden and Thomas*, 2013). Analysis of P-waveforms supports heterogeneity by revealing complex seismic structure near both the eastern and western edges of the Pacific anomaly (*Konishi et al.*, 2014; *Tanaka et al.*, 2015). Also, some regions deep within the LLSVPs appear much slower than expected for purely thermal effects (*To et al.*, 2016).

At somewhat shallower depths, abrupt vertical gradients in v_s may be indicative of large-scale sub-horizontal compositional layering within LLSVPs. These vertical gradients retrieved from waveform-modeling studies occur at heights of ~400 to ~700 km above the CMB beneath the Pacific (*Takeuchi et al.*, 2008; *He and Wen*, 2009), as well as the western flank of the African LLSVP (*Sun and Miller*, 2013), and at up to ~1,200 km above the CMB beneath South/East Africa (*Ni and Helmberger*, 2003; *Wang and Wen*, 2007). Abrupt vertical gradients are here interpreted to occur across interfaces internal to the larger LLSVP domains (i.e., the top of the DDD), because they are often located well within LLSVPs, which extend from the CMB to ~1,800 km above the CMB (Figure 1). This large vertical extent of LLSVPs (or "slow clusters") and large degree of internal variability is supported by cluster analysis of five recent tomography models (*Cottaar and Lekic*, 2016). Also of note is that abrupt vertical gradients roughly coincide with the depth range of pronounced radial changes in LLSVP seismic properties (i.e., constrained by tomography): in terms of average v_s of slow clusters (*Lekic et al.*, 2012), decorrelation of v_s and density (*Mosca et al.*, 2012; *Moulik and Ekström*, 2016), as well as anti-correlation between v_s and v_Φ (*Masters et al.*, 2000; *Romanowicz*, 2001; *Koelemeijer et al.*, 2016; *Tesoniero et al.*, 2016).

We interpret these changes in seismic properties to reflect a compositional boundary within the LLSVPs. Such heterogeneity within LLSVPs may be attributed to various (compositional) models. For example, (1) the LLSVP shallow domains may be composed of basaltic materials (i.e., rock assemblages with a high content of MORB), and the bottom domain (or DDD) of primordial materials, or (2) vice-versa. Alternatively, (3) the LLSVP shallow domain may be made up of hot pyrolite (i.e., purely thermal origin), and the DDD of primordial and/or basaltic materials.

A primordial origin of DDDs such as in scenarios (1) and (3) above is supported by seismic constraints. The observed anti-correlation between v_s and v_Φ in general (*Deschamps et al.*, 2012), and its restriction to the DDDs (*Koelemeijer et al.*, 2016; *Moulik and Ekström*, 2016; *Tesoniero et al.*, 2016) in particular, is best explained by the presence of materials enhanced in Fe-rich bridgmanite, potentially with primordial origin. Based on the spatial distribution of the anti-correlation (*Koelemeijer et al.*, 2016; *Moulik and Ekström*, 2016; *Tesoniero et al.*, 2016), an alternative iso-chemical explanation for the anti-correlation appears require that post-perovskite is stable within the hot DDDs. In turn, Fe-rich $(Mg,Fe)SiO_3$ bridgmanitic materials can account for the observed anomalously high densities and v_Φ in DDDs through the combined effects of Fe on density, and those of $(Mg,Fe)SiO_3$ on bulk modulus and thus v_Φ (*Deschamps et al.*, 2012; *Wolf et al.*, 2015). A relatively high intrinsic bulk modulus can account for the observed anti-correlation, and is consistent with the parameter range spanned by our preferred models (which display positive $\partial \Delta\rho_{PRI}/\partial z$, and thus are more compressible than pyrolite). The formation of materials strongly enhanced in bridgmanite has been indeed linked to primordial processes such as magma-ocean crystallization (*Elkins-Tanton*, 2008), since Mg-rich bridgmanite is the magma-ocean liquidus phase over a wide pressure range (*de Koker et al.*, 2013; *Tateno et al.*, 2014), but a mechanism for subsequent Fe-enrichment remains elusive. Other viable (primordial) candidates for DDD composition involve foundered $CaSiO_3$–rich proto-crust (*Kawai and Tsuchiya*, 2014) as well as anomalously reduced bridgmanitic materials (*Gu et al.*, 2016).

To test whether LLSVP shallow domains are dominantly basaltic (scenario (1) above) as in regimes IIb/IV, or pyrolytic in composition (scenario (3) above) as in regime IIa, we analyze seismic array data. Note that seismic tomography is insufficient to distinguish between these two end-members because of a nearly perfect trade-off between temperature and basalt content when predicting seismic velocities at mid-mantle depths (*Wentzcovitch et al.*, 2010; *Deschamps et al.*, 2012). We focus on the vertical component of arrivals in western North America that are related to events in the western Pacific. We detected signals arriving at the array from a different direction than the main phases of the events. Using the directivity information given by the backazimuth and slowness as well as the travel-time of each signal, the ray-paths and reflection points are reconstructed by back-tracing through a one-dimensional velocity model (we use ak135 (*Kennett et al.*, 1995)). The data processing is explained in detail in *Schumacher and Thomas* (2016). Figure 8a shows the locations of the events (red stars), the reference stations (black triangles), and the reflection points (circles, depth indicated by color) which are able to explain the measured backazimuth, slowness and traveltime of our out-of-plane signals.

Two reflection points are located in the mid mantle below the Pacific at a depth of ~1,500 km. They can be explained by P-to-P underside reflections off the top of the LLSVP shallow domain as predicted by mantle-convection models in regimes IIb and IV. With respect to uncertainties in the back-tracing routine as well as seismic tomography, the two reflection points agree with the upper bound of the low velocity region in the S40RTS tomography model (Fig. 8b). Another two reflection points in the same region are located deeper, well within the interior of the LLSVP, as imaged by tomography, in a depth of around 2250km and 2550km. The observed signals could be caused by P-to-P underside reflections off an internal compositional domain boundary, such as between the DDD and LLSVP shallow domain.

The underside reflections retrieved here thus lend credibility to a double-layered model for LLSVP composition, e.g. with a deep primordial domain and a shallow basaltic domain. In particular, the two reflections at ~1,500 km depth appear to be at odds with a purely-thermal LLSVP shallow domain, indicating a sub-horizontal compositional boundary such as between basaltic materials and ambient-mantle pyrolite. Note that a purely-thermal shallow domain is expected to be structurally dominated by the presence of sub-vertical plumes. Thus, the underside reflections retrieved here corroborate a (thermo-)chemical origin for the whole LLSVPs (deep plus shallow domains) with a total volume of ~8% of the mantle (*Cottaar and Lekic*, 2016). However, future systematic studies of underside reflections are certainly needed to support this interpretation, and to rule out any alternative scenarios. For example, we cannot exclude the possibility that individual reflections are simply caused by the marble-cake structure of the mantle.

Nevertheless, mostly based on the geometry of reflection points, both near the roof and within LLSVPs, we prefer a scenario with hot and compositionally "double-layered" thermochemical piles (Fig. 8). As another line of evidence, note that a reservoir for the long-term (>3 Gyr) storage of subducted (basaltic) materials somewhere in the (lower) mantle is required by hotspot-lava isotope geochemistry (*Cabral et al.*, 2013). If the DDDs are indeed primodial in origin (see above), then the LLSVP shallow domains are perhaps the best candidate to host this reservoir. Along these lines, the predictions of cases in regimes IIb and IV (Figs. 5c, 6) with composite piles of primordial (bottom) and basaltic (shallow domains) materials are most consistent with observations. In an alternative explanation, both LLSVP shallow domains and DDDs host primordial materials, but with a distinct major-element composition in each domain (i.e., different kinds of primordial materials, for example recording different processes). While this scenario is fully consistent with the seismic observations presented here, it does not offer an opportunity for the long-term storage of subducted materials. In any case, as our model results exclusively depend on the material properties modelled, predictions for regimes IIb and IV are also applicable to this alternative scenario.

By visual analysis, cases in regime IV appear to be in better agreement with seismic observations than those in regime IIb, because the volume of basaltic material preserved in the lower mantle is greater. Piles in regime IV extend upward from the CMB to depths of ~1,100 km depth, similar to depths inferred for LLSVP roofs (i.e., on the basis of cluster analysis of, and radial correlation functions of global seismic-tomography models (*Rudolph et al.*, 2015; *Cottaar and Lekic*, 2016); also see Fig. 1). In contrast, thermochemical piles in regime IIb do not extend as much above the CMB due to progressive erosion of basaltic material. Note however that seismic tomography might somewhat overestimate the height of the piles, and more importantly that our geodynamic models do not consider the replenishment of basalt by deep subduction (there is no explicit subduction of basalt in our models). Partial erosion of the basaltic layer over 3 Gyr model time such as predicted by cases in regime IIb can indeed be well compensated by subduction and accumulation of MORB. For modern-style plate tectonics, MORB subduction on the order of $D_{CRUST} \cdot L_{SUBD} \cdot V_{SUBD}$ (with crustal thickness $D_{CRUST} \approx 7$ km, the length of all subduction zones $L_{SUBD} \approx 60{,}000$ km and the average speed of plate convergence $V_{SUBD} \approx 50$ km/Myr) can potentially replenish up to ~7% of the volume of the mantle (i.e., similar to the volume of LLSVPs) per billion year. Considering this flux of subducted MORB, cases in regime IIb with moderate erosion of basaltic materials are equally or perhaps even more realistic than those in regime IV. A mix of ancient and young (i.e., recently replenished) basaltic materials in the lower-mantle source region of mantle plumes is consistent with isotope geochemical constraints (*Sobolev et al.*, 2011a; *Cabral et al.*, 2013).

Another difference between regimes IIb and IV is in the slopes of the pile's sides, which are generally less steep in regime IIb than in regime IV. This difference can be understood if one recalls that regime IIb manifests at lower $\Delta\rho_{BAS,1000}$ (Fig. 4a), and thus usually also at lower $\Delta\rho_{BAS,1000} - \Delta\rho_{BAS,2300}$ (Table 2) than regime IV. The weaker depth-dependence of $\Delta\rho_{BAS}$ acts to reduce the slope of the piles, because the (positive) pile density anomaly (or negative buoyancy) in the deep mantle becomes larger at a given density anomaly at the top of the pile, or in other words, because of a reduced "metastability" (*Tan and Gurnis*, 2007). Cluster analysis of v_s tomographic models shows that LLSVPs consist of aggregations of meso-scale piles that exhibit a wide range of morphologies, from gently or moderately steep slopes, to near vertical or even overhanging (*Cottaar and Lekic*, 2016). This range of topographies is highly consistent with findings from studies of P waves that report regionally varying LLSVP slopes (*Frost and Rost*, 2014). Such regional variations are indeed expected for LLSVPs with pronounced (lateral) compositional heterogeneity.

5. Discussion

The above seismic constraints lend credibility to our models in regimes IIb and IV with composite "double-layered" thermochemical piles (Figs. 6-7). These two regimes are restricted to a rather small parameter range in Figure 4, thus tightly bracketing model parameters. The related bounds for basalt densities in the deep mantle and $\partial\Delta\rho_{BAS}/\partial z$ are generally consistent with mineral-physics estimates (*Ricolleau et al.*, 2010; *Deschamps et al.*, 2012). In terms of the density difference between (primordial?) DDD materials and pyrolite $\Delta\rho_{PRI}$, the models yield bounds of about 160 kg/m^3 to 190 kg/m^3. These latter bounds correspond to relevant buoyancy numbers $B = \Delta\rho/\alpha T_m \rho_0$ of ~1.1 to ~1.3 at the α and T_m assumed here. These B can potentially be used to constrain DDD composition. Even tighter bounds arise from our models for the density difference between basalt and (primordial) DDD materials deep in the mantle (100~120 kg/m^3)

and corresponding *B* (0.7~0.8). Thus, better mineral-physics constraints on basalt density under the relevant high pressure-temperature conditions may help to constrain the density, composition and origin of DDDs. Note however that the above bounds may be sensitive to parameter choices and model assumptions that have not been systematically explored here. For example, we did not consider the effects of intrinsic viscosity variations between the materials, which should influence mixing between materials and thermochemical-pile shapes (e.g., *Bower et al.*, 2013), and thus density anomalies required for a specific regime. Also, we do not explore the rheology of subducted slabs in the deep mantle systematically, or even the history of subduction, which both affect the coupling between the pile(s) and the ambient mantle, and hence pile shapes (e.g., *Steinberger and Torsvik*, 2012; *Bull et al.*, 2014).In regimes IIa and IV, two distinct types of plumes emerge from the LLSVPs (also see chapter 3.2). Hot and stationary plumes rise from the LLSVP margins; somewhat cooler, episodic "plumelets" from LLSVP roofs. These predictions can reconcile characteristic differences between "primary" and "secondary" plumes, as inferred from a range of geophysical and geochemical observations (*Courtillot et al.*, 2003). While primary plumes are thought to ascend from the CMB, secondary plumes (or plumelets) are thought to episodically rise from a thermal boundary layer in the mid-mantle (*Davaille*, 1999; *Tanaka et al.*, 2009; *Saki et al.*, 2015), similar to our model predictions (Fig. 9). For example, age-distance patterns as well as isotope geochemical signatures of South Pacific hotspots (i.e. directly above the Pacific LLSVP) indicate episodic short-lived volcanism (≤20 Myrs) (*Clouard and Bonneville*, 2005; *Jackson et al.*, 2010), whereas e.g. Hawaii, Réunion and Iceland plumes display much longer-lived volcanism (~100 Myrs or more). Accordingly, the rise of plumes both from the margins as well as the roofs of double-layered LLSVPs as predicted by our models can account for the diversity among hotspot volcanism worldwide, for example in terms of plume excess temperatures and buoyancy fluxes (*Sleep*, 1990; *Herzberg et al.*, 2007; *Ballmer et al.*, 2015c). That the rise of plumes is not restricted to LLSVP margins (cf. *Burke et al.*, 2008), but also involves LLSVP roofs, is moreover consistent with statistical assessments of hotspot locations (*Austermann et al.*, 2014; *Davies et al.*, 2015).

The predictions of our models in terms of entrainment of materials in the lower mantle have implications for our understanding of ocean-island basalt (OIB) geochemistry. On average, plumes in our models continuously entrain (and deliver into the asthenosphere) rather small fractions of primordial materials (i.e., ~3% in regime IIb / ~2% in regime IV) in addition to moderate fractions of basaltic material (~14% / ~8%). Entrainment of basaltic and primordial material strongly varies between individual plumes, and over time for the same plume (see also *Deschamps et al.*, 2011; *Williams et al.*, 2015). Both basaltic and primordial materials are more efficiently carried by hot "primary" plumes than by warm "secondary" plumes, consistent with geochemical observations (*Courtillot et al.*, 2003; *Sobolev et al.*, 2007). Since these dense materials are more fusible than pyrolite, and are usually entrained into the hottest core of the plume (*Jones et al.*, 2016), they are expected to be over-represented in mantle melting and associated hotspot lavas (*Phipps Morgan*, 1999; *Ito and Mahoney*, 2005; *Ballmer et al.*, 2013). Strong but variable contributions of basaltic (i.e., mafic) materials are indeed consistent with olivine major-element geochemistry of OIB (*Sobolev et al.*, 2005; 2007; *Herzberg*, 2011). For example, some primary hotspots such as Hawaii or Iceland have much more strongly mafic sources than MORBs (*Sobolev et al.*, 2007). In turn, if noble gases are indeed stored within the primordial DDDs, then they should be more efficiently sampled by primary than by secondary plumes. This prediction is consistent with the highest $^{3}He/^{4}He$ ratios being sampled at e.g. Iceland and Hawaii hotspots. In more general terms, the predicted composite source for OIB volcanism helps to understand the large variability spanned by isotope geochemical data, as well as the intimate association of primordial and recycled geochemical signatures (*Zindler and Hart*, 1986; *Hofmann*, 1997; *Koppers and Staudigel*, 2005; *Garapic et al.*, 2015).

A composite source for OIB volcanism may further provide an explanation for the geochemical asymmetry as is observed across various oceanic hotspot tracks (*Huang et al.*, 2011; *Weis et al.*, 2011; *Payne et al.*, 2013; *Jackson et al.*, 2014; *Hoernle et al.*, 2015). For example, the Hawaiian hotspot is separated into the "Loa" and "Kea" trends with distinct isotopic signatures and contributions from mafic materials in mantle melting (*Abouchami et al.*, 2005; *Sobolev et al.*, 2005). Our calculations in preferred regimes IIb and IV predict "primary" plumes to rise from the margins of double-layered piles and thus to entrain distinct types of materials on either side of the plume (Fig. 7a). On the side facing away from the LLSVP, the plumes tend to entrain hot and mostly pyrolytic material from the thermal boundary layer just above the CMB. On the other side, they are predicted to entrain warm and partly basaltic material (plus some primordial material) from the thermal boundary layer just above the LLSVP flank (including some LLSVP material). These model predictions involve a thermal as well as a compositional gradient across major plumes. Thus, they may provide an explanation for the relationship of geochemical asymmetry across hotspots with the underlying geometry of LLSVPs. However, since superposition of thermal effects and compositional effects during plume ascent (in terms of buoyancy, and fusibility during hotspot melting) may obscure the deep origin of these patterns (*Ballmer et al.*, 2015a; *Jones et al.*, 2016), we motivate petrological studies of lateral thermal variations across hotspots (cf. *Xu et al.*, 2014), in addition to those of lateral isotopic variations.

Double-layering of materials within LLSVPs may moreover provide an explanation for the poor expression of primordial reservoir(s) in hotspot lavas. Whereas ancient noble-gas signatures have been well documented in OIB (*Mukhopadhyay*, 2012), indicating the persistence of reservoir(s) that have formed within ~100 Myrs of Earth accretion, any such evidence from other isotopic systems in modern OIB is still lacking. For example, the ^{182}Hf-^{182}W and ^{146}Sm-^{142}Nd systems should record any early differentiation of the Earth, but until recently any ^{182}W or ^{142}Nd anomalies have only been retrieved from high-precision analyses of Archean igneous rocks (see references in *Brown et al.*, 2014). The lack of evidence from both these systems for modern OIB suggests that any primordial reservoirs, if they indeed persist in the mantle, are rather well hidden. Double-layering of LLSVPs with a bottom layer of primordial material that is shielded by an overlying basaltic layer provides good conditions to promote persistence of primordial materials. Note that our models predict plumes to entrain only very small fractions of primordial material, and that high-precision ^{182}W or ^{142}Nd measurements are yet only available for a small subset of OIBs. Indeed, recent high-precision ^{182}W analyses indicate a primordial contribution to Ontong-Java and North-Atlantic flood basalts (*Rizo et al.*, 2016), supporting our interpretations.

Mapping the internal LLSVP compositional boundary may thus quantify the volume of primordial geochemical reservoirs, with implications for the Earth's chemical budget as well as the distribution of radioactive isotopes through the mantle. According to our hypothesis (Fig. 9), the volume(s) of any (enriched) primordial reservoirs correspond to that of the DDDs, which have been estimated at 2-3% of the mantle's volume (*Hernlund and Houser*, 2008). Primordial reservoir(s) enriched in iron (and thus possibly enriched in other incompatible elements) are viable candidates for DDD composition, because iron-enrichment is required to reconcile DDD physical properties (see above). This interpretation does not rule out any (depleted) primordial reservoir(s) to be dispersed through the ambient mantle (*Becker et al.*, 1999). While the requirement for the survival of a large or strongly-enriched primordial reservoir from early silicate-silicate fractionation (i.e., "early enriched reservoir" (EER) (*Boyet and Carlson*, 2005)) has been removed by a better understanding of ^{142}Nd nucleosynthetic anomalies across the solar nebula (*Bouvier and Boyet*, 2016; *Burkhardt et al.*, 2016), a moderately-enriched primordial reservoir similar in size to that of the DDDs cannot be ruled out at the current precision of ^{142}Nd analyses. Moreover, the survival of a primordial reservoir that records early metal-silicate fractionation due to core formation is evident by the recovered ^{182}W anomalies (see above; *Rizo et al.*, 2016). Independent of the specific origin and composition of any primordial reservoir(s), we speculate that the African LLSVP may contain more primordial (and less basaltic) material (similar to regime IIb?) compared to the Pacific LLSVP (regime IV?), because abrupt gradients tend to be closer to tomographically-inferred LLSVP boundaries (see detailed discussion in *Cottaar and Lekic*, 2016). Such a possible difference in their make-up may account for differences in shapes and volumes of these two major LLSVPs, and is consistent with the recent history of basalt subduction.

We show that layering of materials within LLSVPs with a primordial bottom domain (or DDD) and a basaltic shallow domain is geodynamically viable and can reconcile a range of seismic observations (see sections 3-4). LLSVP bottom layer(s) may host iron-enriched cumulates that have been formed in the upper mantle during the late stages of magma-ocean crystallization, and then foundered to the base of the mantle (*Elkins-Tanton*, 2008; *Brown et al.*, 2014). Alternatively, primordial heterogeneity may have originated from incomplete core-mantle equilibration during multi-stage planetary accretion and core formation (*Kaminski and Javoy*, 2013). The accumulation of subducted MORB on top of such primordial materials likely requires an efficient mechanism of basalt-harzburgite separation somewhere in the mantle. Separation would be driven by the density difference between both these lithologies, but should only be efficient in a region of low viscosities, for example in the mantle transition zone (*Motoki and Ballmer*, 2015) or near the CMB (*Tackley*, 2011), where the stabilization of post-perovskite may reduce viscosity (*Ammann et al.*, 2010). Quantitative integration of seismology, geodynamics and mineral-physics approaches is needed to further constrain the heterogeneous composition and origin of LLSVPs.

6. Conclusion

We here combine two key seismic observations to motivate a geodynamic study of compositional layering within thermochemical piles. First, seismic tomography models agree well with each other, in that LLSVPs are broad features that extend from the CMB upward to ~1,000 km depth (Fig. 1) (*Cottaar and Lekic*, 2016). Second, abrupt vertical gradients of seismic wave speed as well as pronounced radial changes of LLSVP seismic properties (in terms of average v_s, and the correlations between v_s and v_Φ, as well as between v_s and net density) occur at ~2,300 km depth within LLSVPs (see section 4), thereby separating the LLSVPs into a shallow domain and distinct deep domain (DDD). Our geodynamic models demonstrate that two layers with distinct composition and physical properties can avoid significant mixing with each other (and with the rest of the mantle) over billions of years, forming double-layered composite piles in the lower mantle. The parameter space, in which limited mixing occurs and piles with geometries similar to LLSVPs are formed, can inform about the specific compositions and origins of heterogeneity within LLSVPs.

We hypothesize that LLSVP shallow domains are mostly basaltic in composition, and DDDs are primordial in origin. A composition of LLSVP shallow domains that is distinct from the ambient mantle (and likely basaltic) is supported by underside reflections that we detect near LLSVP tops (see section 4). A primordial origin of DDDs is supported by the anti-correlation between v_s and v_Φ as well as the decorellation of v_s and density, as are observed in the deep lower mantle (*Deschamps et al.*, 2012; *Koelemeijer et al.*, 2016; *Moulik and Ekström*, 2016). Such large-scale compositional layering within LLSVPs is reconciled by another set of underside reflections that we detect at 2250-2550 km depth, as well as by published observations of abrupt vertical gradients that occur in a similar depth range. A composite make-up of the LLSVPs overall (Figure 9) is consistent with geochemical constraints for the manifestation of long-lived subduction-related as well as primordial reservoirs somewhere in the (lower) mantle, which are variably tapped by mantle plumes (see section 5). Indeed, our geodynamic models predict mantle plumes to originate from the (1) flanks as well as (2) the roofs of double-layered thermochemical piles, and to entrain a mix of materials. Model predictions in terms of location, vigor, episodicity and materials entrained by these two types of plumes are generally consistent with those inferred from observations for (1) "primary" and (2) "secondary" plumes (*Courtillot et al.*, 2003). Future modeling efforts are required to quantitatively test geodynamic-model predictions with seismic observables as well as geochemical signatures of hotspot lavas.

7. Acknowledgements

We thank Frédéric Deschamps and Mingming Li for their constructive reviews that helped to improve the manuscript, as well as Paula Koelemeijer for inspiring discussions. M.D.B. and G.I. were supported by NSF-grant EAR-1141938; L.S. was supported by DFG-grant TH1530/11-1; V.L. acknowledges support from NSF-grant EAR-1352214, and the Packard Foundation. Calculations were performed on "akua", the in-house cluster of the Department of Geology and Geophysics (Univ. Hawaii).

8. Figures and Tables

Figure 1: Seismic profiles through the (**A**) African and (**B**) Pacific LLSVP. Colors show average S-wave anomalies across five recent tomographic models: SPani (*Tesoniero et al.*, 2016), SAVANI (*Auer et al.*, 2014), S40RTS (*Ritsema et al.*, 2011), "ME2016" (*Moulik and Ekström*, 2016), and UCBSEM-WM1 (*French and Romanowicz*, 2014). Before averaging, all these models were truncated at spherical harmonic degree 18, and had the global average shear-wave speed at each depth removed. (**C**) Horizontal cross-section through the same average S-wave model at 2,800 km depth with profile locations (black lines). Green and white dots mark the left and right sides of each profile, respectively. For cross-sections through cluster analyses of the same five tomography models, see Figures 4-5 in *Cottaar and Lekic* (2016).

Figure 2: Model setup with initial conditions of (**A**) composition and (**B**) temperature. Initial thermal conditions (**B**) are shown as a vertical profile at the left side of the model domain (x = 0 km) that is representative for the whole domain.

Figure 3: Viscosity and compositional density profiles for the reference case A5LE. (**A**) Representative viscosity profile is shown as the horizontal average of viscosity in the reference case A5LE after 3 Gyr model time, and generally consistent with post-glacial rebound, geoid and slab-sinking speed constraints (*Mitrovica and Forte*, 1997; *Čížková et al.*, 2012; *Rudolph et al.*, 2015). (**B**) Depth-dependent compositional density profiles for the basaltic (blue) and primordial (dark brown) materials are given, along with depth-dependent thermal expansivity α (red). The specific parameters $\Delta\rho_{BAS,UM}$, $\Delta\rho_{BAS,CMB}$, $\Delta\rho_{PRI,UM}$, and $\Delta\rho_{PRI,CMB}$ for reference case A5LE are marked by black circles. These parameters alone define the density profiles between cases. Note that the applied parameterization for basaltic material involves that $\Delta\rho_{BAS} = 2\Delta\rho_{BAS,UM}$ at 300-410 km depth and $\Delta\rho_{BAS} = -3\Delta\rho_{BAS,UM}$ at 660-720 km depth (dashed lines).

Figure 4: Regime map (**A**) showing the style of thermochemical convection in the lower mantle for each case as a two-dimensional projection of the four-dimensional parameter space. In this projection, parameters $\boldsymbol{\Delta\rho_{BAS,UM}}$, $\boldsymbol{\Delta\rho_{BAS,CMB}}$, $\boldsymbol{\Delta\rho_{PRI,UM}}$, and $\boldsymbol{\Delta\rho_{PRI,CMB}}$, are expressed in terms of the densities of basaltic material at 1,000 km depth ($\boldsymbol{\Delta\rho_{BAS,1000}}$), and of primordial material at 2,300 km depth ($\boldsymbol{\Delta\rho_{PRI,2300}}$); see text and Figure 3. Numerical experiments can be classified into six different (major and subsidiary) regimes (colors). Filled circles mark cases that are shown in detail in Figs. 5-7. (**B**) Percentage of nearly pure primordial material after 3 Gyrs model time as a function of the density difference between primordial and basaltic materials at 2300 km depth. Preferred regimes IIb and IV (see section 4) require density differences of greater than ~100 kg/m^3.

Figure 5: Snapshots of mantle composition predicted by cases (**A**) X5LH (**B**) 74KF, (**C**) 94KF and (**D**) X5JB after ~3 Gyrs model time. These cases are representative of regimes I, IIa, IIb and III, respectively. Primordial and basaltic materials are denoted white and green, respectively (ambient-mantle pyrolite is blue). All other colors represent mixtures between the materials. Contours of potential temperature (dashed) are spaced at intervals of 200 K.

Figure 6: Snapshots of (**A**) composition and (**B**) potential temperature for the reference case A5LE (regime IV) after 3 Gyrs model time. For color scale and description of dashed lines in (**A**), see Figure 5 caption. Dashed lines in (**B**) roughly delineate compositional domain boundaries contouring mechanical mixtures of 25% primordial with 75% basaltic materials, and 75% basaltic material with 25% pyrolite (see dashed tickmarks in Figure-5-colorscale). For animated versions of panels (**A**) and (**B**), see Movies S1 and S2, respectively.

Figure 7: Snapshots of net-density anomaly for the reference case A5LE (regime IV). For an animated version, see Movie S3. Net density anomalies $\Delta\rho = \rho - \rho_0$ are computed from Eq. (1), and the radial average is removed. Positively and negatively buoyant mantle rocks are visualized by warm and cold colors, respectively. For description of dashed lines, see Figure 5 caption.

Figure 8: Reflection points located in the lower mantle beneath the Pacific. (**A**) Stars and triangles represent the location of events and stations, respectively. The great circle paths are shown as black lines. Plate boundaries (red) are taken from Bird (2003). Reflection points are displayed by circles and their depth is indicated by color (red to blue for shallow to deep points, respectively). (**B**) The cross-section shows the reflection points as black circles superimposed onto the shear wave tomography model S40RTS by Ritsema et al. (2011).

Figure 9: Summary cartoon. LLSVPs are proposed to be compositionally subdivided into two domains, a "primordial" bottom domain and a shallow domain made up of a mix of mostly mafic lithologies (i.e, subducted and accumulated MORB) plus some ultramafic lithologies (tiger stripes). Abrupt seismic gradients, as are found by waveform-modeling studies, are here interpreted to occur across the boundaries between compositional domains, at some of which seismic reflections are also observed (see section 4). Seismic reflections from the LLSVP top boundary are not expected to be coherent (dashed line). Blobs qualitatively mark the entrainment of LLSVP materials by plumes.

Table 1: key model parameters. The bottom four rows report the free parameters of this study (bold) that have been systematically explored within the reported range. ([a]) For definition of depth-dependent parameters, see text and Figure 3b.

Parameter	**symbol**	**value, range**
depth of the numerical domain	z_{box}	2,900 km
width of the numerical domain	x_{box}	8,700 km
surface temperature	T_0	0 ºC
mantle reference potential temperature	T_m	2,000 ºC
mantle reference density	ρ_0	4,500 kg/m^3
mantle reference viscosity	η_0	$1.4\cdot10^{21}$ Pa·s
activation volume	V^*	$1.36114\cdot10^{-6}$ m^3/mol
activation energy	E^*	47,549.97 J/mol
density anomaly related to depletion of pyrolite	$\Delta\rho_F$	[a]
excess density of basaltic material	$\Delta\rho_{BAS}$	[a]
excess density of primordial material	$\Delta\rho_{PRI}$	[a]
thermal expansivity	α	[a]
gravity acceleration	g	9.8 m^2/s
thermal diffusivity	κ	$2.5\cdot10^{-6}$ m^2/s
upper-mantle excess density of basaltic material	$\boldsymbol{\Delta\rho_{BAS,UM}}$	**70 kg/m^3 – 120 kg/m^3**
excess density of basaltic material at CMB	$\boldsymbol{\Delta\rho_{BAS,CMB}}$	**40 kg/m^3 – 80 kg/m^3**
upper-mantle excess density of primordial material	$\boldsymbol{\Delta\rho_{PRI,UM}}$	**160 kg/m^3 – 230 kg/m^3**
excess density of primordial material at CMB	$\boldsymbol{\Delta\rho_{PRI,CMB}}$	**120 kg/m^3 – 200 kg/m^3**

Table 2: Summary of the results for all 67 cases (reference case A5LE is marked by asterisk). Input parameters are reported in italics [kg/m^3]. Important output variables (also used as diagnostic criteria to distinguish between regimes) are given in bold [%]. The "survival rates" of basaltic and primordial materials, $surv_{BAS}$ and $surv_{PRI}$, are computed as the volumes of mantle material with concentrations of basaltic and primordial material exceeding 80% after 3 Ga model time divided by the initial volumes. The area of the CMB covered by primordial material after 3 Ga model time $covrg_{CMB}$ is reported in the last column. $covrg_{CMB}$, $surv_{BAS}$ and $surv_{PRI}$ are used as criteria for discrimination between regimes (see first column). A small subset of cases ([a]) have not been run long enough to reach 3 Ga model time, but note that regime discrimination for these cases is unambiguous upon visual inspection of results.

regime	case	$\Delta\rho_{BAS,660}$	$\Delta\rho_{BAS,CMB}$	$\Delta\rho_{PRI,660}$	$\Delta\rho_{PRI,CMB}$	$\mathbf{surv_{BAS}}$	$\mathbf{surv_{PRI}}$	$\mathbf{covrg_{CMB}}$
I	**97JH**	*90*	*70*	*200*	*180*	**52.0**	**63.3**	**74.2**
I	**X5LH**	*100*	*50*	*220*	*180*	**67.7**	**69.5**	**89.2**
I	**X6KG**	*100*	*60*	*210*	*170*	**61.0**	**65.7**	**73.3**
I	**A5LG**	*110*	*50*	*220*	*170*	**76.0**	**80.1**	**80.3**
I	**A6JH**	*110*	*60*	*200*	*180*	**59.5**	**77.8**	**76**
I	**A6LH**	*110*	*60*	*220*	*180*	**68.5**	**71.0**	**67.2**
I	**A7KG**	*110*	*70*	*210*	*170*	**80.5**	**69.5**	**62.5**
I	**A7LG**	*110*	*70*	*220*	*170*	**74.2**	**69.8**	**80.7**
I	**A8LH**	*110*	*80*	*220*	*180*	**62.7**	**75.4**	**83.9**
I	**B6KF**	*120*	*60*	*210*	*160*	**66.0**	**63.8**	**92.6**
I	**B6KH**	*120*	*60*	*210*	*180*	**85.2**	**79.4**	**60**
I	**B6MH**	*120*	*60*	*230*	*180*	**80.1**	**77.3**	**65.7**
I	**B8KI**	*120*	*80*	*210*	*190*	**85.1**	**82.6**	**100**
I	**B8MI**	*120*	*80*	*230*	*190*	**82.4**	**82.1**	**95.3**
IIa	**00JG**	*0*	*0*	*200*	*170*	**N/A**	**100**	**48**
IIa	**74HD**	*70*	*40*	*180*	*140*	**0.1**	**65.4**	**45.3**
IIa	**74JE**	*70*	*40*	*200*	*150*	[a]	[a]	[a]
IIa	**74JF**	*70*	*40*	*200*	*160*	**0.0**	**99.1**	**36.3**
IIa	**74KF**	*70*	*40*	*210*	*160*	**4.1**	**90.4**	**44.8**
IIa	**77HH**	*70*	*70*	*180*	*180*	**0.0**	**88.0**	**60.6**
IIa	**94JE**	*90*	*40*	*200*	*150*	**0.2**	**63.8**	**27.1**
IIa/III	**87KF**	*80*	*70*	*210*	*160*	**0.0**	**24.7**	**40**
IIa/III	**88JF**	*80*	*80*	*200*	*160*	**0.5**	**24.3**	**31.1**
IIb	**88JJ**	*80*	*80*	*200*	*200*	**15.2**	**63.6**	**54.5**
IIb	**94KF**	*90*	*40*	*210*	*160*	**25.6**	**55.2**	**45.1**
IIb	**94LG**	*90*	*40*	*220*	*170*	**12.1**	**88.5**	**35.2**
IIb	**94MH**	*90*	*40*	*230*	*180*	**36.5**	**56.3**	**57**
IIb	**95JF**	*90*	*50*	*200*	*160*	**11.1**	**50.8**	**28.5**
IIb	**95KG**	*90*	*50*	*210*	*170*	**18.3**	**62.5**	**52**
IIb	**96KF**	*90*	*60*	*210*	*160*	**1.0**	**60.3**	**38.6**
IIb	**97IH**	*90*	*70*	*190*	*180*	**12.2**	**65.8**	**30.4**

IIb	**X5JE**	*100*	*50*	*200*	*150*	**20.5**	**50.6**	**27.2**
IIb	**X5JG**	*100*	*50*	*200*	*170*	**25.3**	**56.4**	**38.1**
IIb	**X5KG**	*100*	*50*	*210*	*170*	**44.7**	**69.0**	**62**
IIb	**X5KH**	*100*	*50*	*210*	*180*	**53.3**	**71.5**	**53.7**
IIb	**X5LI**	*100*	*50*	*220*	*190*	**60.9**	**67.6**	**62.7**
IIb/III	**X4JE**	*100*	*40*	*200*	*150*	**23.4**	**37.4**	**36.2**
IIIa	**88FB**	*90*	*40*	*160*	*120*	**2.4**	**7.5**	**38.8**
IIIa	**94HB**	*90*	*40*	*180*	*120*	**0.4**	**2.4**	**19.7**
IIIa	**94JB**	*90*	*40*	*200*	*120*	**2.8**	**18.8**	**24.4**
IIIa	**X4HB**	*100*	*40*	*180*	*120*	[a]	[a]	[a]
IIIa	**X5HB**	*100*	*50*	*180*	*120*	[a]	[a]	[a]
IIIa	**A5JB**	*110*	*50*	*200*	*120*	**12.2**	**5.8**	**26.2**
IIIa	**A6HB**	*110*	*60*	*180*	*120*	[a]	[a]	[a]
IIIa	**A6HE**	*110*	*60*	*180*	*150*	**38.9**	**18.3**	**34.4**
IIIa	**A6JB**	*110*	*60*	*200*	*120*	**15.1**	**1.5**	**13.6**
IIIb	**94HE**	*90*	*40*	*180*	*150*	**11.1**	**20.5**	**14.6**
IIIb	**X4HD**	*100*	*40*	*180*	*140*	**23.4**	**22.0**	**31.9**
IIIb	**X5IE**	*100*	*50*	*190*	*150*	**43.5**	**45.1**	**32.2**
IIIb	**X5JB**	*100*	*50*	*200*	*120*	**27.0**	**30.1**	**43**
IIIb	**X5JD**	*100*	*50*	*200*	*140*	**36.5**	**40.0**	**55**
IIIb	**A5JE**	*110*	*50*	*200*	*150*	**63.8**	**50.0**	**34.8**
IIIb	**A6JE**	*110*	*60*	*200*	*150*	**48.8**	**42.1**	**48.4**
IIIb	**A7JF**	*110*	*70*	*200*	*160*	**50.8**	**35.9**	**42.9**
IV	**X5HG**	*100*	*50*	*180*	*170*	**43.9**	**53.5**	**43.9**
IV	**X5IF**	*100*	*50*	*190*	*160*	**50.5**	**52.2**	**48**
IV	**X5KE**	*100*	*50*	*210*	*150*	**43.1**	**63.3**	**70.6**
IV	**X6JF**	*100*	*60*	*200*	*160*	**54.4**	**49.3**	**65.7**
IV	**X6KF**	*100*	*60*	*210*	*160*	**53.7**	**60.1**	**66**
IV	**X7IG**	*100*	*70*	*190*	*170*	**47.1**	**63.8**	**59.7**
IV	**X7JH**	*100*	*70*	*200*	*180*	**72.3**	**61.3**	**66.2**
IV	**A5JG**	*110*	*50*	*200*	*170*	**67.8**	**65.5**	**61**
IV	***A5LE**	*110*	*50*	*220*	*150*	**66.5**	**61.0**	**55.9**
IV	**A5LF**	*110*	*50*	*220*	*160*	**63.4**	**67.3**	**49**
IV	**A6JG**	*110*	*60*	*200*	*170*	**64.2**	**64.0**	**55.6**
IV	**A6LG**	*110*	*60*	*220*	*170*	**65.2**	**76.1**	**55.3**
IV	**B6LG**	*120*	*60*	*220*	*170*	**81.7**	**70.2**	**57.9**

9. References

Abouchami, W., A. W. Hofmann, S. J. G. Galer, F. A. Frey, J. Eisele, and M. Feigenson (2005), Lead isotopes reveal bilateral asymmetry and vertical continuity in the Hawaiian mantle plume, *Nature*, *434*(7035), 851-856, doi:10.1038/nature03402.

Ammann, M. W., J. P. Brodholt, J. Wookey, and D. P. Dobson (2010), First-principles constraints on diffusion in lower-mantle minerals and a weak D" layer, *Nature*, *465*(7297), 462-465, doi:10.1038/nature09052.

Aoki, I., and E. Takahashi (2004), Density of MORB eclogite in the upper mantle, *Phys. Earth Planet. Inter.*, *143*, 129-143, doi:10.1016/j.pepi.2003.10.007.

Auer, L., L. Boschi, T. Becker, T. Nissen-Meyer, and D. Giardini (2014), Savani: A variable resolution whole-mantle model of anisotropic shear velocity variations based on multiple data sets, *Journal of Geophysical Research: Solid Earth*, *119*(4), 3006-3034.

Austermann, J., B. T. Kaye, J. X. Mitrovica, and P. Huybers (2014), A statistical analysis of the correlation between large igneous provinces and lower mantle seismic structure, *Geophys. J. Int.*, *197*(1), 1-9, doi:10.1093/gji/ggt500.

Ballmer, M. D., G. Ito, and C. Cheng (2015a), Asymmetric Dynamical Behavior of Thermochemical Plumes and Implications for Hawaiian Lava Composition, in *Hawaiian Volcanoes*, edited, pp. 35-57, John Wiley & Sons, Inc, doi:10.1002/9781118872079.ch3.

Ballmer, M. D., G. Ito, J. van Hunen, and P. J. Tackley (2010), Small-scale sublithospheric convection reconciles geochemistry and geochronology of 'Superplume' volcanism in the western and south Pacific, *Earth Planet. Sci. Lett.*, *290*(1-2), 224-232.

Ballmer, M. D., G. Ito, C. J. Wolfe, and S. C. Solomon (2013), Double layering of a thermochemical plume in the upper mantle beneath Hawaii, *Earth Planet. Sci. Lett.*, *376*, 155-164, doi:10.1016/j.epsl.2013.06.022.

Ballmer, M. D., N. C. Schmerr, T. Nakagawa, and J. Ritsema (2015b), Compositional mantle layering revealed by slab stagnation at ~1000-km depth, *Science Advances*, *1*(11), doi:10.1126/sciadv.1500815.

Ballmer, M. D., J. van Hunen, G. Ito, T. A. Bianco, and P. J. Tackley (2009), Intraplate volcanism with complex age-distance patterns – a case for small-scale sublithospheric convection, *Geochem. Geophys. Geosyst.*, *10*, Q06015, doi:10.1029/2009gc002386.

Ballmer, M. D., P. E. van Keken, and G. Ito (2015c), 7.10 - Hotspots, Large Igneous Provinces, and Melting Anomalies, in *Treatise on Geophysics (Second Edition)*, edited by G. Schubert, pp. 393-459, Elsevier, Oxford.

Becker, T. W., J. B. Kellogg, and R. J. O'Connell (1999), Thermal constraints on the survival of primitive blobs in the lower mantle, *Earth Planet. Sci. Lett.*, *171*, 351-365.

Bird, P. (2003), An updated digital model of plate boundaries, *Geochemistry Geophysics Geosystems*, *4*, 1027.

Bouvier, A., and M. Boyet (2016), Primitive Solar System materials and Earth share a common initial 142Nd abundance, *Nature*, *537*(7620), 399-402, doi:10.1038/nature19351.

Bower, D. J., M. Gurnis, and M. Seton (2013), Lower mantle structure from paleogeographically constrained dynamic Earth models, *Geochemistry Geophysics Geosystems*, *14*(1), 44-63, doi:10.1029/2012gc004267.

Boyet, M., and R. W. Carlson (2005), Nd-142 evidence for early (> 4.53 Ga) global differentiation of the silicate Earth, *Science*, *309*(5734), 576-581, doi:10.1126/science.1113634.

Brandenburg, J. P., and P. E. van Keken (2007), Deep storage of oceanic crust in a vigorously convecting mantle, *Journal of Geophysical Research-Solid Earth*, *112*(B6), 15, doi:10.1029/2006jb004813.

Brown, S. M., L. T. Elkins-Tanton, and R. J. Walker (2014), Effects of magma ocean crystallization and overturn on the development of Nd-142 and W-182 isotopic heterogeneities in the primordial mantle, *Earth Planet. Sci. Lett.*, *408*, 319-330, doi:10.1016/j.epsl.2014.10.025.

Bull, A. L., M. Domeier, and T. H. Torsvik (2014), The effect of plate motion history on the longevity of deep mantle heterogeneities, *Earth Planet. Sci. Lett.*, *401*, 172-182, doi:10.1016/j.epsl.2014.06.008.

Burke, K., B. Steinberger, T. H. Torsvik, and M. A. Smethurst (2008), Plume generation zones at the margins of large low shear velocity provinces on the core-mantle boundary, *Earth Planet. Sci. Lett.*, *265*(1-2), 49-60, doi:10.1016/j.epsl.2007.09.042.

Burkhardt, C., L. E. Borg, G. A. Brennecka, Q. R. Shollenberger, N. Dauphas, and T. Kleine (2016), A nucleosynthetic origin for the Earth's anomalous 142Nd composition, *Nature*, *537*(7620), 394-398, doi:10.1038/nature18956.

Cabral, R. A., M. G. Jackson, E. F. Rose-Koga, K. T. Koga, M. J. Whitehouse, M. A. Antonelli, J. Farquhar, J. M. D. Day, and E. H. Hauri (2013), Anomalous sulphur isotopes in plume lavas reveal deep mantle storage of Archaean crust, *Nature*, *496*(7446), 490-493, doi:10.1038/nature12020.

Caracausi, A., G. Avice, P. G. Burnard, E. Füri, and B. Marty (2016), Chondritic xenon in the Earth's mantle, *Nature*, *533*(7601), 82-85, doi:10.1038/nature17434.

Christensen, U. R., and A. W. Hofmann (1994), Segregation of subducted oceanic crust and the convection mantle, *J. Geophys. Res.*, *99*, 19867-19884.

Čížková, H., A. P. van den Berg, W. Spakman, and C. Matyska (2012), The viscosity of Earth's lower mantle inferred from sinking speed of subducted lithosphere, *Phys. Earth Planet. Inter.*, *200–201*, 56-62, doi:10.1016/j.pepi.2012.02.010.

Clouard, V., and A. Bonneville (2005), Ages of seamounts, islands, and plateaus on the Pacific plate, *Plumes, Plates, and Paradigms, Spec. Pap. Geol. Soc. Am.*, *388*, 71-90.

Cobden, L., and C. Thomas (2013), The origin of D ' reflections: a systematic study of seismic array data sets, *Geophys. J. Int.*, *194*(2), 1091-1118, doi:10.1093/gji/ggt152.

Cottaar, S., and V. Lekic (2016), Morphology of Seismically Slow Lower Mantle Structures, *Geophys. J. Int.*, *in press*, doi:10.1093/gji/ggw324.

Courtillot, V., A. Davaille, J. Besse, and J. Stock (2003), Three distinct types of hotspots in the Earth's mantle, *Earth Plan. Sci. Lett.*, *205*(3-4), 295-308.

Davaille, A. (1999), Simultaneous generation of hotspots and superswells by convection in a heterogeneous planetary mantle, *Nature*, *402*(6763), 756-760.

Davies, D. R., S. Goes, and M. Sambridge (2015), On the relationship between volcanic hotspot locations, the reconstructed eruption sites of large igneous provinces and deep mantle seismic structure, *Earth Planet. Sci. Lett.*, *411*, 121-130, doi:10.1016/j.epsl.2014.11.052.

de Koker, N., B. B. Karki, and L. Stixrude (2013), Thermodynamics of the MgO–SiO 2 liquid system in Earth's lowermost mantle from first principles, *Earth Planet. Sci. Lett.*, *361*, 58-63.

Deschamps, F., L. Cobden, and P. J. Tackley (2012), The primitive nature of large low shear-wave velocity provinces, *Earth Planet. Sci. Lett.*, *349–350*(0), 198-208, doi:10.1016/j.epsl.2012.07.012.

Deschamps, F., E. Kaminski, and P. J. Tackley (2011), A deep mantle origin for the primitive signature of ocean island basalt, *Nature Geosci.*, *4*(12), 879-882, doi:10.1038/ngeo1295.

Deschamps, F., and P. J. Tackley (2008), Searching for models of thermo-chemical convection that explain probabilistic tomography I. Principles and influence of rheological parameters, *Phys. Earth Planet. Inter.*, *171*(1-4), 357-373, doi:10.1016/j.pepi.2008.04.016.

Deschamps, F., and J. Trampert (2004), Towards a lower mantle reference temperature and composition, *Earth Planet. Sci. Lett.*, *222*(1), 161-175, doi:10.1016/j.epsl.2004.02.024.

Doubrovine, P. V., B. Steinberger, and T. H. Torsvik (2016), A failure to reject: Testing the correlation between large igneous provinces and deep mantle structures with EDF statistics, *Geochemistry, Geophysics, Geosystems*, *17*(3), 1130-1163, doi:10.1002/2015GC006044.

Dziewonski, A. M., V. Lekic, and B. A. Romanowicz (2010), Mantle Anchor Structure: An argument for bottom up tectonics, *Earth Planet. Sci. Lett.*, *299*(1-2), 69-79, doi:10.1016/j.epsl.2010.08.013.

Elkins-Tanton, L. T. (2008), Linked magma ocean solidification and atmospheric growth for Earth and Mars, *Earth Planet. Sci. Lett.*, *271*(1-4), 181-191, doi:10.1016/j.epsl.2008.03.062.

Elkins-Tanton, L. T., P. C. Hess, and E. M. Parmentier (2005), Possible formation of ancient crust on Mars through magma ocean processes, *J. Geophys. Res.*, *110*(E12S01), doi:10.1029/2005JE002480.

French, S. W., and B. A. Romanowicz (2014), Whole-mantle radially anisotropic shear velocity structure from spectral-element waveform tomography, *Geophys. J. Int.*, *199*(3), 1303-1327, doi:10.1093/gji/ggu334.

Frost, D. A., and S. Rost (2014), The P-wave boundary of the Large-Low Shear Velocity Province beneath the Pacific, *Earth Planet. Sci. Lett.*, *403*, 380-392, doi:10.1016/j.epsl.2014.06.046.

Garapic, G., A. Mallik, R. Dasgupta, and M. G. Jackson (2015), Oceanic lavas sampling the high-He-3/He-4 mantle reservoir: Primitive, depleted, or re-enriched?, *American Mineralogist*, *100*(10), 2066-2081, doi:10.2138/am-2015-5154.

Gerya, T. V., and D. A. Yuen (2003), Characteristics-based marker-in-cell method with conservative finite-differences schemes for modeling geological flows with strongly variable transport properties, *Physics of the Earth & Planetary Interiors*, *140*(4), 293-318.

Gu, T., M. Li, C. McCammon, and K. K. M. Lee (2016), Redox-induced lower mantle density contrast and effect on mantle structure and primitive oxygen, *Nature Geosci*, *advance online publication*, doi:10.1038/ngeo2772.

He, Y., and L. Wen (2009), Structural features and shear-velocity structure of the "Pacific Anomaly", *Journal of Geophysical Research-Solid Earth*, *114*, doi:10.1029/2008jb005814.

Hernlund, J. W., and C. Houser (2008), The statistical distribution of seismic velocities in Earth's deep mantle, *Earth Planet. Sci. Lett.*, *265*(3-4), 423-437, doi:10.1016/j.epsl.2007.10.042.

Hernlund, J. W., and A. K. McNamara (2015), 7.11 - The Core–Mantle Boundary Region A2 - Schubert, Gerald, in *Treatise on Geophysics (Second Edition)*, edited, pp. 461-519, Elsevier, Oxford, doi:10.1016/B978-0-444-53802-4.00136-6.

Herzberg, C. (2011), Identification of source lithology in the Hawaiian and Canary Islands: implications for origins, *J. Petrol.*, *52*(1), 113-146, doi:10.1093/petrology/egq075.

Herzberg, C., P. D. Asimow, N. Arndt, Y. L. Niu, C. M. Lesher, J. G. Fitton, M. J. Cheadle, and A. D. Saunders (2007), Temperatures in ambient mantle and plumes: constraints from basalts, picrites, and komatiites, *Geochem. Geophys. Geosyst., 8*, 34, doi:10.1029/2006gc001390.

Hirose, K., F. Yingwei, M. Yanzhang, and M. Ho-Kwang (1999), The fate of subducted basaltic crust in the Earth's lower mantle, *Nature*, *397*(6714), 53-56.

Hoernle, K., J. Rohde, F. Hauff, D. Garbe-Schoenberg, S. Homrighausen, R. Werner, and J. P. Morgan (2015), How and when plume zonation appeared during the 132 Myr evolution of the Tristan Hotspot, *Nature Communications*, *6*, doi:10.1038/ncomms8799.

Hofmann, A. W. (1997), Mantle geochemistry: the message from oceanic volcanism, *Nature*, *385*(6613), 219-229.

Huang, S., P. S. Hall, and M. G. Jackson (2011), Geochemical zoning of volcanic chains associated with Pacific hotspots, *Nature Geoscience*, *4*(12), 874-878, doi:10.1038/ngeo1263.

Ishii, M., and J. Tromp (1999), Normal-mode and free-air gravity constraints on lateral variations in velocity and density of Earth's mantle, *Science*, *285*(5431), 1231-1235.

Ito, G., and J. J. Mahoney (2005), Flow and melting of a heterogeneous mantle: 1.Method and importance to the geochemistry of ocean island and mid-ocean ridge basalts, *Earth Planet. Sci. Lett.*, *230*, 29-46.

Jackson, M. G., S. R. Hart, J. G. Konter, A. A. P. Koppers, H. Staudigel, M. D. Kurz, J. Blusztajn, and J. M. Sinton (2010), Samoan hot spot track on a "hot spot highway": Implications for mantle plumes and a deep Samoan mantle source, *Geochemistry Geophysics Geosystems*, *11*, doi:10.1029/2010gc003232.

Jackson, M. G., S. R. Hart, J. G. Konter, M. D. Kurz, J. Blusztajn, and K. A. Farley (2014), Helium and lead isotopes reveal the geochemical geometry of the Samoan plume, *Nature*, *514*(7522), 355-+, doi:10.1038/nature13794.

Jones, T. D., D. R. Davies, I. H. Campbell, C. R. Wilson, and S. C. Kramer (2016), Do mantle plumes preserve the heterogeneous structure of their deep-mantle source?, *Earth Planet. Sci. Lett.*, *434*, 10-17, doi:10.1016/j.epsl.2015.11.016.

Kaminski, E., and M. Javoy (2013), A two-stage scenario for the formation of the Earth's mantle and core, *Earth Planet. Sci. Lett.*, *365*, 97-107, doi:10.1016/j.epsl.2013.01.025.

Kawai, K., and R. J. Geller (2010), Waveform inversion for localized seismic structure and an application to D″ structure beneath the Pacific, *Journal of Geophysical Research: Solid Earth*, *115*(B1), n/a-n/a, doi:10.1029/2009JB006503.

Kawai, K., and T. Tsuchiya (2014), P-V-T equation of state of cubic CaSiO3 perovskite from first-principles computation, *Journal of Geophysical Research-Solid Earth*, *119*(4), 2801-2809, doi:10.1002/2013jb010905.

Kennett, B. L. N., E. R. Engdahl, and R. Buland (1995), Constraints On Seismic Velocities in the Earth From Travel-Times, *Geophys. J. Int.*, *122*(1), 108-124.

Koelemeijer, P., A. Deuss, and J. Ritsema (in review), Density structure of Earth's lowermost mantle from Stoneley mode splitting observations.

Koelemeijer, P., J. Ritsema, A. Deuss, and H. J. van Heijst (2016), SP12RTS: a degree-12 model of shear- and compressional-wave velocity for Earth's mantle, *Geophys. J. Int.*, *204*(2), 1024-1039, doi:10.1093/gji/ggv481.

Konishi, K., K. Kawai, R. J. Geller, and N. Fuji (2014), Waveform inversion for localized three-dimensional seismic velocity structure in the lowermost mantle beneath the Western Pacific, *Geophys. J. Int.*, *199*(2), 1245-1267, doi:10.1093/gji/ggu288.

Koppers, A. A. P., and H. Staudigel (2005), Asynchronous bends in Pacific seamount trails: A case for extensional volcanism?, *Science*, *307*(5711), 904-907, doi:10.1126/science.1107260.

Labrosse, S., J. W. Hernlund, and N. Coltice (2007), A crystallizing dense magma ocean at the base of the Earth's mantle, *Nature*, *450*, 866-869, doi:10.1038/nature06355.

Lay, T., J. Hernlund, and B. A. Buffett (2008), Core-mantle boundary heat flow, *Nature Geoscience*, *1*(1), 25-32, doi:10.1038/ngeo.2007.44.

Lekic, V., S. Cottaar, A. Dziewonski, and B. Romanowicz (2012), Cluster analysis of global lower mantle tomography: A new class of structure and implications for chemical heterogeneity, *Earth Planet. Sci. Lett.*, *357–358*, 68-77, doi:10.1016/j.epsl.2012.09.014.

Li, M., A. K. McNamara, and E. J. Garnero (2014), Chemical complexity of hotspots caused by cycling oceanic crust through mantle reservoirs, *Nature Geosci*, *7*(5), 366-370, doi:10.1038/ngeo2120.

Lin, S. C., and P. E. van Keken (2005), Multiple volcanic episodes of flood basalts caused by thermochemical mantle plumes, *Nature*, *436*(7048), 250-252, doi:10.1038/nature03697.

Masters, G., G. Laske, H. Bolton, and A. Dziewonski (2000), The relative behavior of shear velocity, bulk sound speed, and compressional velocity in the mantle: Implications for chemical and thermal structure., in *Geophysical Monograph on Mineral Physics and Seismic Tomography fom the atomic to the global scale*, edited by S. Karato, A. M. Forte, R. C. Liebermann, G. Masters and L. Stixrude, pp. 63-87, Americal Geophysical Union.

McNamara, A. K., E. J. Garnero, and S. Rost (2010), Tracking deep mantle reservoirs with ultra-low velocity zones, *Earth Planet. Sci. Lett.*, *299*(1-2), 1-9, doi:10.1016/j.epsl.2010.07.042.

McNamara, A. K., and S. Zhong (2005), Thermochemical piles beneath Africa and the Pacific Ocean, *Nature*, *437*, 1136-1139.

Mitrovica, J. X., and A. M. Forte (1997), Radial Profile Of Mantle Viscosity - Results From the Joint Inversion Of Convection and Postglacial Rebound Observables, *Journal Of Geophysical Research Solid Earth*, *102*(B2), 2751-2769.

Moresi, L., and M. Gurnis (1996), Constraints on the lateral strength of slabs from 3-dimensional dynamic flow models, *Earth Planet. Sci. Lett.*, *138*(1-4), 15-28.

Mosca, I., L. Cobden, A. Deuss, J. Ritsema, and J. Trampert (2012), Seismic and mineralogical structures of the lower mantle from probabilistic tomography, *J. Geophys. Res.*, *117*, B06304, doi:10.1029/2011jb008851.

Motoki, M. H., and M. D. Ballmer (2015), Intraplate volcanism due to convective instability of stagnant slabs in the Mantle Transition Zone, *Geochemistry, Geophysics, Geosystems*, doi:10.1002/2014GC005608.

Moulik, P., and G. Ekström (2016), The relationships between large-scale variations in shear velocity, density, and compressional velocity in the Earth's mantle, *Journal of Geophysical Research: Solid Earth*, *121*(4), 2737-2771.

Mukhopadhyay, S. (2012), Early differentiation and volatile accretion recorded in deep-mantle neon and xenon, *Nature*, *486*(7401), 101-U124, doi:10.1038/nature11141.

Nakagawa, T., and B. A. Buffett (2005), Mass transport mechanism between the upper and lower mantle in numerical simulations of thermochemical mantle convection with multicomponent phase changes, *Earth Planet. Sci. Lett.*, *230*, 11-27.

Nakagawa, T., and P. J. Tackley (2005), The interaction between the post-perovskite phase change and a thermo-chemical boundary layer near the core-mantle boundary, *Earth Planet. Sci. Lett.*, *238*, 204-216.

Nakagawa, T., and P. J. Tackley (2014), Influence of combined primordial layering and recycled MORB on the coupled thermal evolution of Earth's mantle and core, *Geochemistry, Geophysics, Geosystems*, *15*(3), 619-633, doi:10.1002/2013GC005128.

Nakagawa, T., P. J. Tackley, F. Deschamps, and J. A. D. Connolly (2010), The influence of MORB and harzburgite composition on thermo-chemical mantle convection in a 3-D spherical shell with self-consistently calculated mineral physics, *Earth Planet. Sci. Lett.*, *296*(3-4), 403-412, doi:10.1016/j.epsl.2010.05.026.

Ni, S., E. Tan, M. Gurnis, and D. V. Helmberger (2002), Sharp sides to the African superplume, *Science*, *296*, 1850-1852.

Ni, S. D., and D. V. Helmberger (2003), Ridge-like lower mantle structure beneath South Africa, *Journal of Geophysical Research-Solid Earth*, *108*(B2), doi:10.1029/2001jb001545.

Nomura, R., K. Hirose, K. Uesugi, Y. Ohishi, A. Tsuchiyama, A. Miyake, and Y. Ueno (2014), Low Core-Mantle Boundary Temperature Inferred from the Solidus of Pyrolite, *Science*, *343*(6170), 522-525, doi:10.1126/science.1248186.

Payne, J. A., M. G. Jackson, and P. S. Hall (2013), Parallel volcano trends and geochemical asymmetry of the Society Islands hotspot track, *Geology*, *41*(1), 19-22, doi:10.1130/g33273.1.

Peto, M. K., S. Mukhopadhyay, and K. A. Kelley (2013), Heterogeneities from the first 100 million years recorded in deep mantle noble gases from the Northern Lau Back-arc Basin, *Earth Planet. Sci. Lett.*, *369*, 13-23, doi:10.1016/j.epsl.2013.02.012.

Phipps Morgan, J. (1999), Isotope topology of individual hotspot basalt arrays: Mixing curves or melt extraction trajectories?, *Geochem. Geophys. Geosyst.*, *1*, 1003, doi:10.1029/1999GC000004.

Ricolleau, A., J.-P. Perrillat, G. Fiquet, I. Daniel, J. Matas, A. Addad, N. Menguy, H. Cardon, M. Mezouar, and N. Guignot (2010), Phase relations and equation of state of a natural MORB: Implications for the density profile of subducted oceanic crust in the Earth's lower mantle, *Journal of Geophysical Research: Solid Earth*, *115*(B8), n/a-n/a, doi:10.1029/2009JB006709.

Ritsema, J., A. Deuss, H. J. van Heijst, and J. H. Woodhouse (2011), S40RTS: a degree-40 shear-velocity model for the mantle from new Rayleigh wave dispersion, teleseismic traveltime and normal-mode splitting function measurements, *Geophys. J. Int.*, *184*(3), 1223-1236, doi:10.1111/j.1365-246X.2010.04884.x.

Rizo, H., R. J. Walker, R. W. Carlson, M. F. Horan, S. Mukhopadhyay, V. Manthos, D. Francis, and M. G. Jackson (2016), Preservation of Earth-forming events in the tungsten isotopic composition of modern flood basalts, *Science*, *352*(6287), 809-812.

Romanowicz, B. (2001), Can we resolve 3D density heterogeneity in the lower mantle?, *Geophys. Res. Lett.*, *28*(6), 1107-1110.

Rudolph, M. L., V. Lekić, and C. Lithgow-Bertelloni (2015), Viscosity jump in Earth's mid-mantle, *Science*, *350*(6266), 1349-1352, doi:10.1126/science.aad1929.

Saki, M., C. Thomas, S. E. Nippress, and S. Lessing (2015), Topography of upper mantle seismic discontinuities beneath the North Atlantic: the Azores, Canary and Cape Verde plumes, *Earth Planet. Sci. Lett.*, *409*, 193-202.

Schumacher, L., and C. Thomas (2016), Detecting lower mantle slabs beneath Asia and the Aleutians, *Geophys. J. Int.*, doi:10.1093/gji/ggw098.

Simmons, N. A., A. M. Forte, L. Boschi, and S. P. Grand (2010), GyPSuM: A joint tomographic model of mantle density and seismic wave speeds, *Journal of Geophysical Research-Solid Earth*, *115*, doi:10.1029/2010jb007631.

Sleep, N. H. (1990), Hotspots and mantle plumes - some phenomenology, *J. Geophys. Res.*, *95*(B5), 6715-6736.

Sobolev, A. V., A. W. Hofmann, K. P. Jochum, D. V. Kuzmin, and B. Stoll (2011a), A young source for the Hawaiian plume, *Nature*, *476*(7361), 434-U483, doi:10.1038/nature10321.

Sobolev, A. V., et al. (2007), The amount of recycled crust in sources of mantle-derived melts, *Science*, *316*(5823), 412-417, doi:10.1126/science.1138113.

Sobolev, A. V., A. W. Hofmann, S. V. Sobolev, and I. K. Nikogosian (2005), An olivine-free mantle source of Hawaiian shield basalts, *Nature*, *434*(7033), 590-597, doi:10.1038/nature03411.

Sobolev, S. V., A. V. Sobolev, D. V. Kuzmin, N. A. Krivolutskaya, A. G. Petrunin, N. T. Arndt, V. A. Radko, and Y. R. Vasiliev (2011b), Linking mantle plumes, large igneous provinces and environmental catastrophes, *Nature*, *477*(7364), 312-316, doi:10.1038/nature10385.

Steinberger, B., and T. H. Torsvik (2012), A geodynamic model of plumes from the margins of Large Low Shear Velocity Provinces, *Geochemistry Geophysics Geosystems*, *13*, Q01w09, doi:10.1029/2011gc003808.

Su, W.-j., and A. M. Dziewonski (1997), Simultaneous inversion for 3-D variations in shear and bulk velocity in the mantle, *Phys. Earth Planet. Inter. (Netherlands)*, *100*(1-4), 135-156.

Sun, D., and M. S. Miller (2013), Study of the western edge of the African Large Low Shear Velocity Province, *Geochemistry, Geophysics, Geosystems*, *14*(8), 3109-3125, doi:10.1002/ggge.20185.

Tackley, P. J. (2011), Living dead slabs in 3-D: The dynamics of compositionally-stratified slabs entering a “slab graveyard” above the core-mantle boundary, *Phys. Earth Planet. Inter.*, *188*(3), 150-162.

Tackley, P. J. (2012), Dynamics and evolution of the deep mantle resulting from thermal, chemical, phase and melting effects, *Earth-Science Reviews*, *110*(1–4), 1-25, doi:10.1016/j.earscirev.2011.10.001.

Takeuchi, N., Y. Morita, N. D. Xuyen, and N. Q. Zung (2008), Extent of the low-velocity region in the lowermost mantle beneath the western Pacific detected by the Vietnamese Broadband Seismograph Array, *Geophys. Res. Lett.*, *35*(5), doi:10.1029/2008gl033197.

Tan, E., and M. Gurnis (2005), Metastable superplumes and mantle compressibility, *Geophys. Res. Lett.*, *32*(20), doi:10.1029/2005gl024190.

Tan, E., and M. Gurnis (2007), Compressible thermochemical convection and application to lower mantle structures, *Journal of Geophysical Research-Solid Earth*, *112*(B6), doi:10.1029/2006jb004505.

Tanaka, S., H. Kawakatsu, M. Obayashi, Y. J. Chen, J. Ning, S. P. Grand, F. Niu, and J. Ni (2015), Rapid lateral variation of P-wave velocity at the base of the mantle near the edge of the Large-Low Shear Velocity Province beneath the western Pacific, *Geophys. J. Int.*, *200*(2), 1050-1063, doi:10.1093/gji/ggu455.

Tanaka, S., D. Suetsugu, H. Shiobara, H. Sugioka, T. Kanazawa, Y. Fukao, G. Barruol, and D. Reymond (2009), On the vertical extent of the large low shear velocity province beneath the South Pacific Superswell, *Geophys. Res. Lett.*, *36*, -, doi:doi:10.1029/2009gl037568.

Tateno, S., K. Hirose, and Y. Ohishi (2014), Melting experiments on peridotite to lowermost mantle conditions, *Journal of Geophysical Research: Solid Earth*, *119*(6), 4684-4694.

Tesoniero, A., F. Cammarano, and L. Boschi (2016), S−to−P heterogeneity ratio in the lower mantle and thermo-chemical implications, *Geochemistry, Geophysics, Geosystems*, *17*(7), 2522-2538, doi:10.1002/2016GC006293.

Thorne, M. S., Y. Zhang, and J. Ritsema (2013), Evaluation of 1-D and 3-D seismic models of the Pacific lower mantle with S, SKS, and SKKS traveltimes and amplitudes, *Journal of Geophysical Research: Solid Earth*, *118*(3), 985-995, doi:10.1002/jgrb.50054.

To, A., Y. Capdeville, and B. Romanowicz (2016), Anomalously low amplitude of S waves produced by the 3D structures in the lower mantle, *Phys. Earth Planet. Inter.*, *256*, 26-36.

To, A., B. Romanowicz, Y. Capdeville, and N. Takeuchi (2005), 3D effects of sharp boundaries at the borders of the African and Pacific Superplumes: Observation and modeling, *Earth Planet. Sci. Lett.*, *233*(1-2), 137-153, doi:10.1016/j.epsl.2005.01.037.

Tolstikhin, I. N., J. D. Kramers, and A. W. Hofmann (2006), A chemical Earth model with whole mantle convection: The importance of a core-mantle boundary layer (D") and its early formation, *Chem. Geol.*, *226*, 79-99.

Torsvik, T. H., K. Burke, B. Steinberger, S. J. Webb, and L. D. Ashwal (2010), Diamonds sampled by plumes from the core-mantle boundary, *Nature*, *466*(7304), 352-355, doi:10.1038/nature09216.

Torsvik, T. H., M. A. Smethurst, K. Burke, and B. Steinberger (2006), Large igneous provinces generated from the margins of the large low-velocity provinces in the deep mantle, *Geophys. J. Int.*, doi:10.1111/j.1365-1246X.2006.03158.x.

Tosi, N., D. A. Yuen, N. de Koker, and R. M. Wentzcovitch (2013), Mantle dynamics with pressure- and temperature-dependent thermal expansivity and conductivity, *Phys. Earth Planet. Inter.*, *217*, 48-58, doi:10.1016/j.pepi.2013.02.004.

Trampert, J., F. Deschamps, J. Resovsky, and D. Yuen (2004), Probabilistic tomography maps chemical heterogeneities throughout the lower mantle, *Science*, *306*(5697), 853-856.

van Hunen, J., S. J. Zhong, N. M. Shapiro, and M. H. Ritzwoller (2005), New evidence for dislocation creep from 3-D geodynamic modeling of the Pacific upper mantle structure, *Earth Plan. Sci. Lett.*, *238*(1-2), 146-155.

Wang, Y., and L. Wen (2007), Geometry and P and S velocity structure of the "African Anomaly", *Journal of Geophysical Research-Solid Earth*, *112*(B5), doi:10.1029/2006jb004483.

Weis, D., M. O. Garcia, J. M. Rhodes, M. Jellinek, and J. S. Scoates (2011), Role of the deep mantle in generating the compositional asymmetry of the Hawaiian mantle plume, *Nature Geosci.*, *4*(12), 831-838, doi:10.1038/ngeo1328.

Wentzcovitch, R. M., Y. G. Yu, and Z. Wu (2010), Thermodynamic Properties and Phase Relations in Mantle Minerals Investigated by First Principles Quasiharmonic Theory, in *Theoretical and Computational Methods in Mineral Physics: Geophysical Applications*, edited by R. Wentzcovitch and L. Stixrude, pp. 59-98, doi:10.2138/rmg.2010.71.4.

Williams, C. D., M. Li, A. K. McNamara, E. J. Garnero, and M. C. van Soest (2015), Episodic entrainment of deep primordial mantle material into ocean island basalts, *Nat Commun*, *6*, doi:10.1038/ncomms9937.

Wolf, A. S., J. M. Jackson, P. Dera, and V. B. Prakapenka (2015), The thermal equation of state of (Mg, Fe)SiO3 bridgmanite (perovskite) and implications for lower mantle structures, *Journal of Geophysical Research: Solid Earth*, *120*(11), 7460-7489, doi:10.1002/2015JB012108.

Workman, R. K., and S. R. Hart (2005), Major and trace element composition of the depleted MORB mantle (DMM), *Earth Planet. Sci. Lett.*, *231*, 53-72.

Xie, S., and P. J. Tackley (2004), Evolution of U-Pb and Sm-Nd systems in numerical models of mantle convection, *J. Geophys. Res.*, *109, B11204*, doi:10.1029/2004JB003176.

Xu, G., S. Huang, F. A. Frey, J. Blichert-Toft, W. Abouchami, D. A. Clague, B. Cousens, J. G. Moore, and M. H. Beeson (2014), The distribution of geochemical heterogeneities in the source of Hawaiian shield lavas as revealed by a transect across the strike of the Loa and Kea spatial trends: East Molokai to West Molokai to Penguin Bank, *Geochimica et Cosmochimica Acta*, *132*(0), 214-237, doi:10.1016/j.gca.2014.02.002.

Xu, W., C. Lithgow-Bertelloni, L. Stixrude, and J. Ritsema (2008), The effect of bulk composition and temperature on mantle seismic structure, *Earth Planet. Sci. Lett.*, *275*(1-2), 70-79, doi:10.1016/j.epsl.2008.08.012.

Zhong, S. (2006), Constraints on thermochemical convection of the mantle from plume heat flux, plume excess temperature, and upper mantle temperature, *J. Geophys. Res.*, *111*(B04409), doi:10.1029/2005JB003972.

Zindler, A., and S. Hart (1986), Helium: problematic primordial signals, *Earth Planet. Sci. Lett.*, *79*(1-2), 1-8.